Optical control of single excitons in semiconductor quantum dots

2014 Semicond. Sci. Technol. 29 053001

(http://iopscience.iop.org/0268-1242/29/5/053001)

IOP Publishing Semiconductor Science and Technology
Semicond. Sci. Technol. **29** (2014) 053001 (23pp) doi:10.1088/0268-1242/29/5/053001

Tutorial

Optical control of single excitons in semiconductor quantum dots

Y Kodriano, E R Schmidgall, Y Benny and D Gershoni

The Department of Physics and the Solid State Institute, Technion-Israel Institute of Technology, Haifa 32000, Israel

E-mail: dg@physics.technion.ac.il

Received 8 September 2013, revised 30 January 2014
Accepted for publication 24 February 2014
Published 28 March 2014

Abstract

The fundamental building block of quantum information processing technologies is the quantum-bit a 'qubit.' These technologies require the ability to prepare, control, and read out a qubit state. Spins confined in self-assembled quantum dots are promising candidates for a quantum bit, because semiconductors are compatible with mature modern opto- and micro-electronics. These quantum dot systems offer two more advantages: they are excellent interfaces between the spin state—an anchored qubit and a photon—a 'flying qubit' and they provide means to coherently control the spin qubit by ultrashort optical pulses. In this review, we thoroughly discuss the qubit provided by an optically-excited electron in a quantum dot–the exciton qubit. We demonstrate its spin state initialization, coherent control and read-out using ultrashort optical pulses.

Keywords: quantum dots, excitons, quantum optics, quantum information processing, optical spectroscopy

(Some figures may appear in colour only in the online journal)

1. Introduction

The field of quantum computing and quantum information processing has generated substantial interest in the past three decades. Quantum computers promise to solve certain problems much faster than is currently possible with classical computing, such as Shor's algorithm for factorizing large numbers [1] and Grover's algorithm for searching databases [2]. In the field of quantum communication, secure, commercial quantum key distribution [3, 4] was demonstrated in an intracompany fibre optic network in Vienna [5]. However, a fully scalable quantum computer has not yet been demonstrated.

The basic building block of quantum information is a qubit [6, 7], a quantum state of the logical one and zero,

$$\psi = \alpha|0\rangle + \beta|1\rangle \qquad |\alpha|^2 + |\beta|^2 = 1. \tag{1}$$

In contrast to a classical bit, the qubit can be in a superposition of $|0\rangle$ and $|1\rangle$, enabling the simultaneous calculation of the outcome of a function for both logical values. To implement a quantum computer, these qubits need to be well-defined and scalable [7]. It must be possible to initialize the qubit system in a known pure state. The performance of quantum computations requires a universal set of gates. A universal set of operations for quantum computation can be constructed from a complete set of single qubit controls—the SU(2) rotations group–and another two qubit gate, such as the controlled not [7–10]. Such multi-qubit gates have been demonstrated experimentally in ion traps [11], atoms [12], superconducting qubits [13], and linear optics [14]. The implementation of these quantum gates requires that the coherence time of the qubit be substantially longer than the gate time [7]. Qubit-specific measurement is necessary to read out the result of the computations [7]. Quantum communications applications require, in addition, the ability to transfer a state between a stationary qubit and a travelling qubit and to then transmit these qubits to distributed locations [7]. A physical quantum computer will probably consist of matter 'anchored' qubits for information storage and processing, with an interface to 'flying' photonic qubits that will carry the information.

There are several candidates for the physical implementations of qubits, reviewed by Ladd *et al* in

[15]. The most promising candidates are ions in electrical traps [16], neutral atoms in optical lattices [17], nuclear magnetic resonances of molecules in liquid solutions [18, 19], superconducting circuits [20], nitrogen-vacancy centres in diamond [21] and charge carrier spins in semiconductor quantum dots (QDs) [22], which are the main focus of the present review.

Semiconductor QDs, frequently referred to as 'artificial atoms' [23–26], are confinement regions for charge carriers in semiconductors. In electrically defined QDs, the confinement of a two dimensional electron gas is created by applying voltage to lithographically defined metallic gates [27, 28]. Recent attempts to define QDs in a double quantum well using gate structures have also been successful [29]. Self-assembled QDs (SAQDs) are nanometric regions of low bandgap semiconductor surrounded by another, higher bandgap semiconductor.

As opposed to electrically defined QDs, SAQDs confine both types of carriers-electrons and holes-making direct bandgap QDs optically active and particularly efficient. The recombination of a confined electron-hole pair, an exciton, in a single SAQD results in the emission of a single photon. Thus, a single optically active QD is a single photon source [30–35]. Moreover, it has been experimentally demonstrated that the cascaded emission from a biexciton in a single QD is a source of entangled photon pairs, since the first emitted photon is entangled with the spin of the remaining exciton [36–38]. Entanglement between a photon emitted from a QD and the spin of a confined electron in the QD has been demonstrated experimentally [39–41], as well as entanglement between two QDs [42]. More recently, teleportation of the quantum state from a photon into a QD spin state [43] has also been demonstrated. Mature semiconductor processing and fabrication technologies make it possible to embed SAQDs into photonic structures, making them very efficient quantum light sources [44, 45].

The spin state of an electron in a SAQD is a two level system that can serve as a qubit. The control of a QD confined electron spin, a single qubit operation, was recently demonstrated through the coupling of an electron to a trion state consisting of two electrons and a hole by the use of an off-resonant laser pulse that created a stimulated Raman transition [46, 47]. The accumulation of a geometric phase through a 2π-area laser pulse was proposed as an alternative method of coherent control [48, 49], and was experimentally demonstrated on multiple QD spins locked into the same transition energy [50], on a single QD electron spin [51], and on the spin configuration of two electrons in a pair of vertically stacked QDs [52]. Coherent control of the confined hole has also been demonstrated [53, 54]. Table 1 summarizes the lifetime and coherence times of the electron spin, hole spin, and the neutral exciton.

In all of these works, complete coherent control is achieved by a set of two sequential optical pulses. The coherent evolution of the precessing spins between the pulses is an essential part of the electron control scheme. This is due to the fact that the trion is composed of two Kramers degenerate states, where each electron spin state is coupled to one of the trion states through either a right or left circularly polarized photon. The result is that the optical control can be performed only in these polarizations. A neutral exciton has a whole integer total spin. In contrast to the electron, it can be coupled to biexcitonic levels with zero angular momentum which have no degeneracy. In this system, the optical control can be in any arbitrary polarization, consequently enabling complete control of the exciton spin with a single pulse [59]. Thus, the duration of the control operation is reduced to that of the laser pulse and is not related to the precession period of the two level system. Here we mainly review complete coherent control of the SAQD exciton as an anchored qubit, using a single optical pulse.

Table 1. Lifetimes and coherence times for spin qubits in a self-assembled semiconductor QD.

	Lifetime		Coherence time	
	Without B field	With B field	Without B field (T_2^*)	With B field (T_2)
Electron [27, 47, 55]	10s of μs	10s of ms	1–10 ns	Few μs
Heavy hole [50, 53, 54, 56]	$\sim$1 μs	Few ms	1–20 ns	10s of μs
Bright exciton [57, 58]	$\sim$1 ns	$>$1 ns	1 ns	$>$1 ns

This review is organized as follows:

Section 2 presents a very brief introduction to QDs and their energy states. In section 3, we briefly review the growth process for SAQDs. Section 4 outlines experimental techniques that can be used to study the single SAQD system and to probe the dynamics of confined carriers. Section 5 discusses more fully the energy levels and spin states of a neutral SAQD, presenting both a theoretical and experimental analysis. Optical initialization of a QD spin state is presented in section 6, and two different methods of optical control of the exciton qubit are presented in sections 7 and 8.

2. Quantum dot states: bright states, dark states, and photoluminescence

QDs consist of a potential well that confines electrons in the conduction band and holes in the valance band of a semiconductor. An electron-hole pair is called an exciton. When the electron and hole spins are antiparallel, the exciton can recombine radiatively and emit a photon. This process is called photoluminescence (PL), and states that are able to recombine radiatively or that can be formed by absorption of a photon, are called *bright* states. When the electron and hole spins are parallel, radiative recombination is not possible and the states are referred to as *dark* states. Two excitons form a biexciton. Charged states are also possible, where a negatively charged state has more electrons than holes and a positively charged state has more holes than electrons [60, 61].

There is a correspondence between the spin state of QD-confined charge carriers, and the polarization of the photon emitted upon recombination of these carriers [57]. Recombination of a $\Uparrow\downarrow$ exciton results in a right-hand

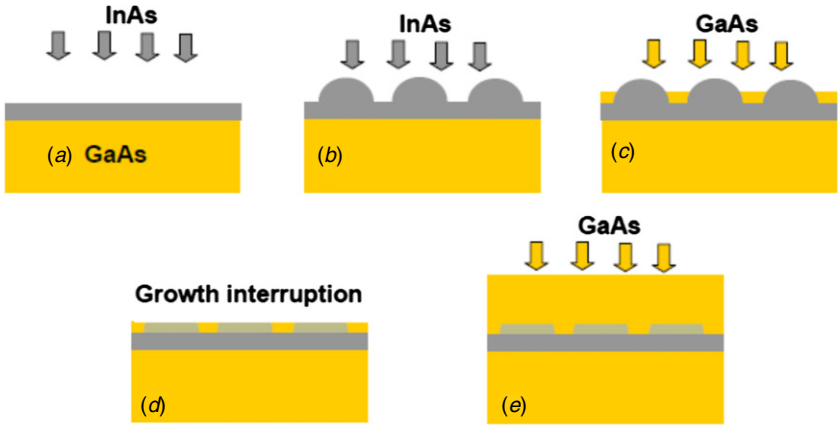

Figure 1. Schematic drawing of the PCI growth technique, a variation of the Stranski–Krastanow QD growth process. (*a*) Deposition of InAs on a GaAs substrate. (*b*) As deposition continues, droplets form. (*c*) A GaAs layer of known width is deposited. (*d*) The deposition is stopped, and diffusion occurs. (*e*) The deposition is resumed, and the QDs are capped by a GaAs layer.

circularly polarized (R) photon carrying the energy released by the pair recombination. Recombination of a $\Downarrow\uparrow$ exciton emits a left-hand circularly polarized (L) photon. Horizontal and vertical polarization are linear combinations of R and L; up to a normalization coefficient they can be written as $H = R+L$ and $V = R - L$. Diagonal (D) and anti-diagonal (B) polarized photons are shifted by a phase: $D = R + \mathrm{i}L$ and $B = R - \mathrm{i}L$. SAQDs tend to have a slight elliptical structure in the plane of the sample, and this structure itself provides a reference axis for linear polarizations. Horizontally (vertically) polarized light is parallel to the major (minor) axis of the QD.

Similarly to atoms, the lowest energy level in a QD has an orbital wavefunction whose spatial part has no nodes. Consequently, we refer to this state as the ground state or s level. The spatial wavefunction for the first excited state has one node, similar to that of a p atomic orbital, so we refer to these levels as p levels or excited states. There are multiple p energy levels in the QD. Since the QD height is usually very small relative to its in-plane dimensions, the p_z levels are substantially higher in energy than the in-plane p_H (node on the major (H) axis) and p_V (node on the minor (V) axis) energy levels. This deviation from cylindrical symmetry removes the degeneracy between p_H and p_V, but their energy splitting remains on the order of the carrier exchange interaction.

The energy of the emitted photon depends on what other carriers are present in the QD. Consequently, the energy of the emitted photons can be used to determine the initial and final population of the QD, and the polarization of the emitted photon provides information about the QD spin configuration. This information is used in techniques called polarization-sensitive PL spectroscopy and photoluminescence excitation (PLE) spectroscopy to characterize QD states and to study the dynamics of photo-excited carriers in QDs.

3. Growth of self-assembled quantum dots

SAQDs are grown using molecular beam epitaxy (MBE). MBE is a technique for growing semiconductor thin films on substrates. This process occurs in an ultra high vacuum system to minimize impurities in the resulting films. Ultra pure elements are heated in separate furnaces until they begin to evaporate or sublime. The atomic or molecular gases are then allowed into the substrate chamber where they adhere to the substrate and react with other atoms on the surface. The rate of deposition is kept low and the film is effectively grown layer by layer. In MBE systems, the layer thickness can be monitored with reflection high-energy electron diffraction (RHEED) [62], allowing for precise control of the layer thickness. RHEED can also be used to monitor the shape and density of the deposited QDs [62, 63].

One of the most common methods for growing QDs with MBE is the Stranski–Krastanow mode (figure 1) [64–66]. This method relies upon the lattice mismatch between different semiconductor crystal structures, such as GaAs and InAs. The bulk lattice structure of InAs differs from the bulk structure of GaAs, in that the lattice constant of InAs is significantly larger (∼8%) than the lattice constant of GaAs. When InAs is grown by MBE on a GaAs substrate, the initial InAs layer (called the wetting layer) will form with the same lattice parameters as the bulk material. This causes a strain in the InAs layer, and this strain energy increases with InAs layer thickness. After a critical thickness is reached, the InAs will form three-dimensional islands of material as opposed to a two-dimensional film. These islands have an increased surface energy and a decreased strain energy, and the island size is spatially limited through the minimization of the total energy. In the case of InAs on a GaAs substrate, the critical thickness is 1.5 monolayers of InAs, or about 4 Å [67]. As the QDs form independently, as a consequence of the lattice mismatch between the two materials, QDs grown by this method are referred to as self-assembled Stranski–Krastanow QDs. In order for Stranski–Krastanow growth to be possible, the lattice mismatch must be greater than about 2%. Several combinations of semiconductors satisfy this requirement, such as GaAs/InAs, SiGe, InAs/InP, and GaInN/GaN.

As a result of the growth process, there will be variation in the geometric and optical properties of the various SAQDs on the substrate. The QD size, height, and composition are all variable, though careful control of the growth conditions can reduce the fluctuations in QD size to <10% [67]. The density

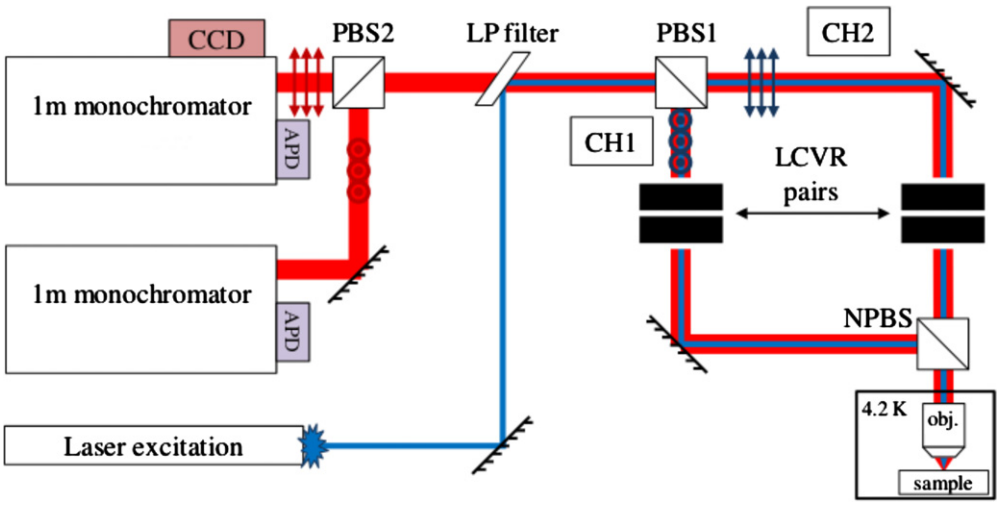

Figure 2. Schematic description of the low temperature polarization sensitive μ-PL setup.

of the QDs is controlled by varying the coverage of InAs on top the GaAs substrate [68, 69]. Changing the MBE growth rate or temperature changes the QD sizes, density, and composition [70]. The optical properties of the QDs can also be changed by postgrowth thermal annealing [71, 72].

The height of the QDs can be controlled using the partially covered island (PCI) growth technique [73] (figure 1). Here, after InAs islands start to form on the GaAs substrate, a GaAs spacer layer of known thickness is deposited on the sample, following which the sample growth process is paused. InAs above the height of the GaAs spacer layer is desorbed, and diffusion of In out of and Ga into the islands changes the chemical composition of the new QDs [74]. The QD height determines the smallest confinement scale of carriers inside the QDs, thus enabling the tunability of the QDs emission energy [73].

In order to enhance the collection efficiency of light emitted from a single QD, the QD layer can be embedded in the middle of a one-wavelength microcavity formed by two sets of distributed Bragg reflectors (DBRs) with a one-wavelength thick GaAs layer between them. The DBRs are composed of stacked pairs of quarter wavelength thick AlAs/GaAs layers. Such a structure enhances the collection efficiency of emitters coupled to the cavity mode. A QD resonant with cavity emits into the cavity mode, directly into the collection lens [75]. This results in the enhancement of the collected intensity from QDs resonant with the cavity mode.

Stopping the rotation of the sample during the growth of the strained InAs layer results in a variable density of QDs across the sample surface [35]. Isolation of a single QD can be achieved by taking advantage of both this variable surface density and the properties of the microcavity. The microcavity limits the energies at which photon collection is possible. Therefore, the density of QDs emitting efficiently in the microcavity is approximately two orders of magnitude lower than their actual density on the sample [75]. If the as-grown density is 10^8 cm^{-2}, the density of QDs resonant with the microcavity is thus $\sim 10^6$ cm^{-2} and single QDs separated by a few tens of micrometers can be easily located by scanning the sample surface during PL measurements [76].

4. Experimental techniques for optical analysis of single quantum dots

4.1. Polarization-sensitive single quantum dot spectroscopy

Figure 2 schematically describes a low temperature polarization-sensitive micro-PL (μ-PL) setup. In a PL experiment, the sample is excited by a laser whose energy is above the bandgap, populating the QD under investigation with hot carriers. These carriers relax to their ground state in the QD, and then upon radiative recombination of an electron-hole pair, a photon is emitted. Recording the polarized emission spectrum reveals information on the exciton ground state energies and the polarization selection rules for recombination.

Polarization control can be achieved by the use of two liquid crystal variable retarders (LCVRs) positioned in the mutual optical path of the excitation laser and collected emission. An LCVR induces a voltage controlled phase, ranging from zero to 2π, to the polarization of light parallel to its extraordinary (fast) axis. The effect of an LCVR on incident laser light can be described as a rotation around the LCVR fast axis on the Poincaré sphere. In figure 2, the first LCVR fast axis lies 45° from the laser polarization, which is the same as the polarizing beam splitter (PBS), and the second is parallel to that polarization. This configuration provides the ability to rotate a polarized laser beam to any desired elliptic polarization or to project the emitted PL on any desired measurement polarization.

Here, the incoming laser is passed through a PBS, marked as PBS1 in figure 2. The light polarized transverse to the plane of incidence (*s*-polarized) is reflected by the PBS to the optical path denoted CH1 while the light polarized in the plane of incidence (*p*-polarized) is transmitted to the path denoted CH2. Thus, by the choice of the laser linear polarization, either *s* or *p*, one can choose through which polarizing arm the laser will pass, or through both. The two arms are combined back together by the use of a non-polarizing beam-splitter (NPBS) and then focused on the sample by an objective with high numerical aperture. The cryostat system is used to cool the QD to the desired temperature, often in the range of 4–20 K.

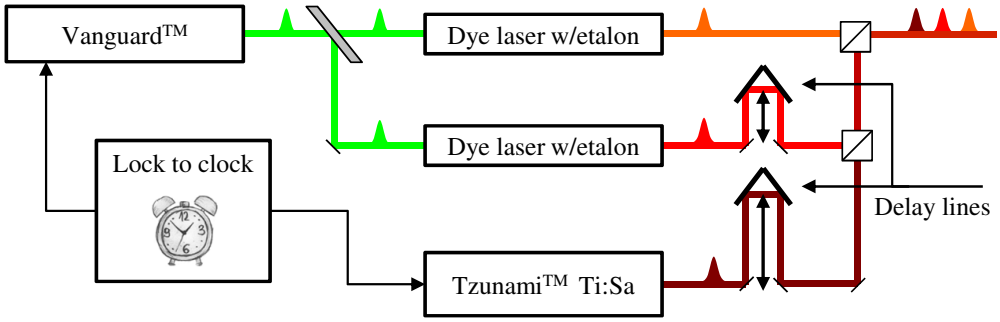

Figure 3. Time-resolved spectroscopy with three pulsed lasers. Here, two dye lasers are driven by the same pump laser, Vanguard, to which is locked a third laser, a Ti:Saph Tsunami laser. The relative timing of pulses in the pulse sequence is varied by the use of delay lines. In this setup, three synchronized pulses of three different energies can be used in a 'write-control-read' experiment.

The emitted PL is collected by the same objective, where the high numerical aperture allows the collection of photons emitted to most of the upper hemisphere (85%). This collection is translated to both increased spatial resolution and also to a wider spectral window of light collected from the microcavity sample [75]. The emitted PL is then split by the NPBS to the two polarizing arms. The LCVR pairs rotate the polarization of the emitted light such that at each arm the measured polarization is now parallel to either the *p*-polarization at CH1 or the *s*-polarization at CH2. The two paths are now combined by PBS1 and the reflected laser is filtered by a long-pass interference filter.

The PL emission is now projected onto another PBS (PBS2 in figure 2) where each of the *s*- and *p*-polarizations are passed to a different meter-long monochromator where the spectrum can be recorded either by a charge coupled device or a fast avalanche photodiode. This setup enables the measurement of two independent polarizations from two independent spectral regions during the same experiment.

4.2. Photoluminescence excitation spectroscopy

As mentioned above, the ground state recombination energies are probed in a PL experiment. In order to probe optical transitions to excited states in the QD, we use PLE measurements. In such experiments, the excitation energy of the laser is varied while the emission at a certain recombination energy is recorded. Enhancement in the recorded signal with respect to the laser energy reveals the transition energies of the excited excitonic states while the polarization of both excitation and emission reveal the polarized absorption selection rules [57, 61, 76]. Both continuous-wave (CW) and pulsed excitation can be used.

4.3. Time-resolved spectroscopy

In some experiments, the temporal evolution of the optically excited QD is investigated. In order to conduct these experiments, two or three synchronous pulsed lasers are used, where the delay between the lasers is varied by a mechanical delay line as displayed in figure 3. The first resonant polarized pulse initializes the state of the QD, while a second, delayed, resonant pulse probes the state of the QD after various time delays. The two pulses are usually not resonant to the same transition, enabling the probing of the excited population. In section 8.1, for example, an intermediate pulse is introduced to the sample. In these experiments, two of the lasers are tuned to the same energy. In order to probe the effect of only a single laser, lock-in detection can be used, with an optical chopper on the path of the one relevant laser.

4.4. Polarization-sensitive correlation measurements

The second-order intensity correlation function between two spectral lines a and b is defined as

$$g^{(2)}(\tau) = \frac{\langle I_a(t) I_b(t+\tau)\rangle}{\langle I_a(t)\rangle \langle I_b(t)\rangle} \tag{2}$$

where $I_{a(b)}$ is the intensity of the given spectral line and $\langle\rangle$ means averaged over time t [77].

In a *radiative cascade,*the emission of multiple photons is correlated. Detecting one of the photons increases the probability of detecting the other photons. If states A and B are connected in a radiative cascade, where a is the spectral line corresponding to the transition from A and b is the spectral line corresponding to the transition from B, I_b at time $t+\tau$ depends on the intensity I_a at the earlier time t. The emission intensity $I_a(t)$ is proportional to the probability that the system is in state A, $P_A(t)$. Emission of a photon from line a at time t sets the system to the final state of the relevant optical transition. Therefore, we can write $\langle I_a(t) I_b(t+\tau)\rangle = \langle I_a(t)\rangle \langle I_{b|a}(t+\tau)\rangle$ where $\langle I_{b|a}(t+\tau)\rangle$ is the intensity of transition b at time $t+\tau$ *conditional* on the system being in the final state of transition a. Equation (2) consequently becomes

$$g^{(2)}(\tau) = \frac{\langle I_a(t)\rangle \langle I_{b|a}(t+\tau)\rangle}{\langle I_a(t)\rangle \langle I_b(t)\rangle} = \frac{\langle I_{b|a}(t+\tau)\rangle}{\langle I_b(t)\rangle} = \frac{P_{B|A}(\tau)}{P_B^{SS}} \tag{3}$$

where $P_{B|A}$ is the population of state B at time τ given that at time zero, the system was in state A and P_B^{SS} is the steady state population of B (i.e. $P_B(\tau \to \infty)$). If the states A and B form a radiative cascade, then the value of $g^{(2)}(\tau)$ should be greater than 1 for some range of times $\tau > 0$ because the transition from state A increases the population in state B to a value above the steady state expectation value. This increase in $g^{(2)}(\tau)$ is called *photon bunching*, and is used to check if two spectral transitions are related via a radiative cascade [78–80].

If $A = B$, the function $g^{(2)}(\tau)$ is referred to as the intensity autocorrelation function. The second-order intensity autocorrelation function is used to check if a source is a

single photon emitter [77]. Since two photons cannot be emitted at the same time from a single photon emitter, for $\tau = 0$, either I_a or I_b is zero, resulting in $g^{(2)}(0) = 0$. More generally, $g^{(2)}(\tau = 0) \sim 1 - 1/n$ where n is the number of photons emitted at $\tau = 0$. For a single photon emitter, $n = 0 \rightarrow g^{(2)}(0) = 0$. In practice, due to the finite temporal resolution of the detectors, the value observed is nonzero but less than 1. This decrease in $g^{(2)}(\tau)$ is called *photon antibunching*. Observation of photon antibunching identified QDs as single photon emitters [32, 33, 35, 81–83].

Charging processes can also lead to the observation of photon bunching between spectral lines [84]. Measurements of $g^{(2)}(\tau)$ can be used to check if two photons are entangled [36] and to study the dynamics of the system in time or in response to a control laser pulse. These techniques were used to study the dynamics of the bright and dark excitons [85].

This second-order intensity correlation function is measured experimentally using a Hanbury Brown and Twiss apparatus [86]. This apparatus provides the necessary means to temporally correlate between the emission intensities of two spectral lines, each one of them projected onto any desired polarization state.

The apparatus is schematically described in figure 2. The time difference between the pulses from the two detectors, described in figure 2, is repeatedly measured using a time to analogue converter. A multi channel analyser then builds a histogram of time differences between the detection times of the two photons. This histogram converges to the intensity correlation function (up to the temporal resolution of the detectors and normalization) as the statistics of the experiment grow. In CW measurements the histogram can be straightforwardly normalized by its value at long time differences.

5. Spin states of a neutral self-assembled quantum dot

5.1. Energy levels of a neutral quantum dot—ground and excited levels

The wavefunctions of single carriers in semiconductor nanostructures can be calculated in various ways, starting for example with simple one band approximations through multiple band $k \cdot p$-like approximations [87, 88] to many atom models [89], in which the actual knowledge of the arrangement of the atoms in the nanostructure is required. Depending on the complexity of the model, the calculated wavefunctions are then usually known numerically only. The precision to which one needs to know these wavefunctions in order to calculate the Coulomb and exchange interactions between carriers occupying single carrier levels requires enormous computer resources. Moreover, the intuition gained in these calculations is rather limited. For these reasons, we decided to describe the QD using a simple parabolic one-band model for the electrons and the heavy holes. Such a model results in analytical expressions for these carrier wavefunctions. Since in (In,Ga)As QDs, strain and quantum size effects separate the light holes band from that of the heavy holes, this approximation can be justified. In this simple model, the QD is represented as an infinite parabolic potential that acts separately on the electrons and the holes [90]. The envelope wavefunctions (orbitals) are given by the 2D harmonic solutions

$$\Psi^{p}_{n_x,n_y}(x,y) = \frac{H_{n_x}\left(\frac{x}{l^x_p}\right)H_{n_y}\left(\frac{y}{l^y_p}\right)}{\sqrt{2^{(n_x+n_y)}n_x!n_y!\pi\, l^x_p l^y_p}} \cdot \mathrm{e}^{-\frac{1}{2}\left[\left(\frac{x}{l^x_p}\right)^2+\left(\frac{y}{l^y_p}\right)^2\right]} \quad (4)$$

where $p = e(h)$ stands for electron (heavy hole) and $H_{n_{x(y)}}$ are the Hermite polynomials of order $n_{x(y)}$. The extent of the potential along the $x-$ ($y-$) direction is described by a characteristic length $l^{x(y)}_p = \sqrt{\hbar/M^*_{\perp,p}\omega^{x(y)}_p}$. This characteristic length $l^{x(y)}_p$ is related to the in-plane effective mass of the charge carrier, $M^*_{\perp,p}$, and the harmonic potential inter-level separation $\hbar\omega^{x(y)}_p$.

Once the eigenenergies and envelope wavefunctions for the single carriers are computed, the many-carrier energies and states are calculated using the configuration interaction (CI) method [10, 30, 91]. A more detailed description of the CI model that we used, which includes also electron-hole exchange interaction can be found in [60].

To describe the states in the QD, the following notation system [76] will be used in the rest of this tutorial. A single carrier state will be first described by its envelope wavefunction or orbital mode, $O = 1, 2, \ldots, 6$. The number represents the energy order of the level, where $O = 1$ represents the ground state, $O = 2$ the first excited state and so forth. The O number is followed by a letter indicating the type of the carrier, electron (e) or heavy hole (h). A superscript to this letter describes the occupation of the single carrier state. A superscript can be either 1 for an open shell or 2 for a closed shell, subject to the Pauli exclusion principle. Non-occupied states are omitted in this notation. Subscripts indicate the mutual spin configuration (σ) of occupied states of carriers of the same type.

5.2. The neutral exciton

The ground exciton state, $X^0_{1,1} \equiv |(1e^1)(1h^1)\rangle$, or X^0 for short, is a two-carrier state, formed primarily[1] by one electron and one heavy hole in their respective ground states. The exchange interaction couples the spins of the electron and the hole, resulting in the observed excitonic fine structure. Using the method of invariants [92], the exchange interaction between the electron and the hole is described by the spin Hamiltonian [60, 93, 94]

$$H_{X^0_{1,1}} = \sum_{i=x,y,z}\left(a^{1,1}_i S^{(e)}_i S^{(h)}_i + b^{1,1}_i S^{(e)}_i S^{3(h)}_i\right), \quad (5)$$

where $S^{(e)}_i$ ($S^{(h)}_i$) represents the ith Cartesian component of the electron (hole) spin, and $a^{1,1}$ ($b^{1,1}$) is the spin–spin coupling constant. The total spin projection on the ith direction is given by $J_i = S^{(e)}_i + S^{(h)}_i$. In matrix form, the basis $|S^{(e)}_z\rangle \otimes |S^{(h)}_z\rangle$ is given by

$$\begin{aligned} |-1/2, 3/2\rangle &= \downarrow^1\Uparrow^1 \quad J_z = 1 \\ |1/2, -3/2\rangle &= \uparrow^1\Downarrow^1 \quad J_z = -1 \\ |1/2, 3/2\rangle &= \uparrow^1\Uparrow^1 \quad J_z = 2 \\ |-1/2, -3/2\rangle &= \downarrow^1\Downarrow^1 \quad J_z = -2 \end{aligned} \quad (6)$$

[1] The complete wave function also has components from other excited carrier states. However, the major part of the wave function (>95%) is composed from carriers in the ground state.

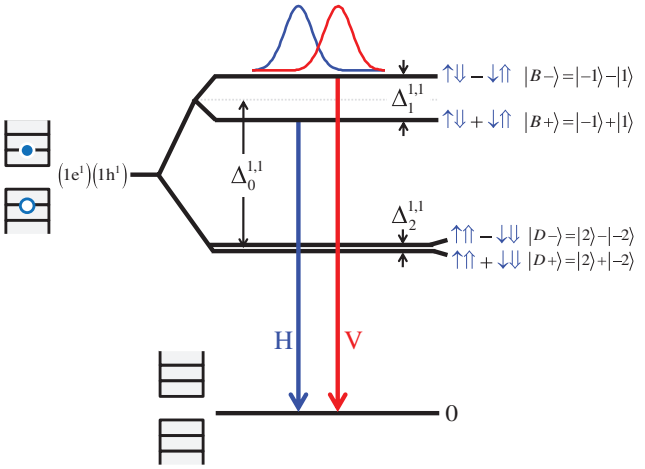

Figure 4. Schematic description of the energy levels of the $|(1e^1)(1h^1)\rangle$ exciton and the allowed optical transitions from exciton states to the vacuum. The major parts of the spin wavefunctions are described to the right of each level. $\uparrow(\Downarrow)$ represents an electron (hole) with spin up (down) and a blue symbol represents a carrier in its ground level. A blue (red) vertical arrow represents linearly polarized optical transition along the major (H) (minor (V)) axis of the QD. The bracketed numbers are the total spin projection of the carriers along the QD growth direction. Image from [76].

where $\uparrow^j$ ($\Downarrow^j$) indicates a spin up (down) electron (heavy hole) in the jth orbital, and the Hamiltonian is given by

$$H_{X^0_{1,1}} = \frac{1}{2}\begin{pmatrix} \Delta_0^{1,1} & \Delta_1^{1,1} & 0 & 0 \\ \Delta_1^{1,1} & \Delta_0^{1,1} & 0 & 0 \\ 0 & 0 & -\Delta_0^{1,1} & \Delta_2^{1,1} \\ 0 & 0 & \Delta_2^{1,1} & -\Delta_0^{1,1} \end{pmatrix} \quad (7)$$

where $\Delta_0^{1,1} = 3(a_z^{1,1} + 2.25b_z^{1,1})$, $\Delta_1^{1,1} = 1.5(b_x^{1,1} - b_y^{1,1})$ and $\Delta_2^{1,1} = 1.5(b_x^{1,1} + b_y^{1,1})$ [93]. The three constants, $\Delta_{0,1,2}^{1,1}$, fully characterize the exchange interaction between the ground state charge carriers [92].

The degeneracy between the four possible combinations of the electron-hole pair spin states is completely removed by the exchange interaction. Figure 4 schematically illustrates the eigenenergies and eigenstates of this electron-hole pair. The four states are split into two doublets, one corresponding to the dark exciton and one corresponding to the bright exciton. The two states of the dark exciton form the lower doublet, $|X^0_{1,1,D_\pm}\rangle \equiv \frac{1}{\sqrt{2}}|[(1e^1)_{1/2}(1h^1)_{3/2} \pm (1e^1)_{-1/2}(1h^1)_{-3/2}]\rangle$. These two states are split by $\Delta_2^{1,1}$. $\Delta_2^{1,1}$ is known to be quite small and believed to be orbit-independent [92]. From the temporal period of the coherent precession of the dark exciton spin, $\Delta_2^{1,1}$ has been measured to be 1.4 μeV [85].

Bright exciton energy states contain an electron and heavy-hole with anti-parallel spins. These states lie $\Delta_0^{1,1}$ above the dark exciton states. The isotropic e-h exchange, $\Delta_0^{1,1}$, is about 300 μeV, as determined from magneto-optical measurements [95]. The anisotropic e-h exchange, $\Delta_1^{1,1}$, splits the symmetric and antisymmetric bright exciton states,

$$|X^0_{1,1,B\pm}\rangle \equiv \frac{1}{\sqrt{2}}|[(1e^1)_{-1/2}(1h^1)_{3/2} \pm (1e^1)_{1/2}(1h^1)_{-3/2}]\rangle. \quad (8)$$

Polarization-sensitive PL spectroscopy can be used to directly measure the magnitude and sign of $\Delta_1^{1,1} = -34$ μeV in the QD used extensively as an example in this tutorial. Since $\Delta_1^{1,1}$ is negative, the antisymmetric state is higher in energy than the symmetric one [60, 94].

When a $\downarrow\Uparrow$ ($\uparrow\Downarrow$) e-h pair recombines radiatively, the conserveration of angular momentum requires emission of a right- (left-) hand circularly polarized photon. It then follows that radiative recombination from the antisymmetric (symmetric) bright exciton state is linearly polarized vertically (V) (horizontally (H)) along the minor (major) in-plane axis of the QD [92, 96]. The four states of the neutral exciton discussed above are not unique to the first single carrier levels ($Oe = Oh = 1$). Instead, any combination of Oe and Oh single carrier states forms similar bright and dark 'excitonic' states. In general, $\Delta_{0,1,2}^{Oe,Oh}$ depends on the orbital mode of the carriers [60, 94].

5.3. The neutral biexciton

The ground biexciton state is formed primarily by two spin-paired heavy holes and two spin-paired electrons in their ground states, $|XX^0_{1,1,1,1}\rangle \equiv |(1e^2)(1h^2)\rangle$. Since, due to the Pauli exclusion principle, the spin-paired carriers can only form an antisymmetric spin singlet state, the σ subscript is redundant and is omitted from the spin state description of the pair. However, for unpaired carriers such as those found in excited biexcitonic states, the spin configuration can be either an antisymmetric singlet or a symmetric triplet state. To indicate the singlet state, the σ subscript is S. To indicate the triplet state, the subscript σ is T_m, where m is the total spin projection along the QD growth direction. For a pair of electrons (heavy holes), m can take the values of 0 or ± 1 (0 or ± 3). The full description of a biexciton with two unpaired electrons and two unpaired holes is

$$\left|XX^0_{O_{e1},O_{e2},O_{h1},O_{h2},\sigma_e,\sigma_h}\right\rangle \equiv (O_{e1}e^1O_{e2}e^1)_{\sigma_e}(O_{h1}h^1O_{h2}h^1)_{\sigma_h}. \quad (9)$$

This set of four unpaired spatial coordinates results in 16 different states with different spin configurations. The 16 states can be divided into four subgroups. There is one state where the two heavy holes form a singlet (h-singlet) and the two electrons also form a singlet (e-singlet). This state is similar in nature to the ground biexciton state, which is also an e-singlet/h-singlet state. Next, there are three states in which the holes form an h-triplet and the electrons an e-singlet (e-singlet/h-triplet). Likewise, there are three possible states in which the holes form a h-singlet and the electrons an e-triplet (e-triplet/h-singlet). Finally, there are nine possible states in which both the holes and the electrons form triplets (e-triplet/h-triplet). Due to the exchange interactions between carriers of the same type, these four subgroups have different energies. The lowest energy levels include the nine e-triplet/h-triplet states. The two intermediate energy levels include the six e-singlet/h-triplet and e-triplet/h-singlet states. The highest energy level is the single e-singlet/h-singlet state. The full mapping of the biexcitonic states is beyond the scope of this tutorial. There are, however, two states which are used extensively in the QD exciton spin control experiments

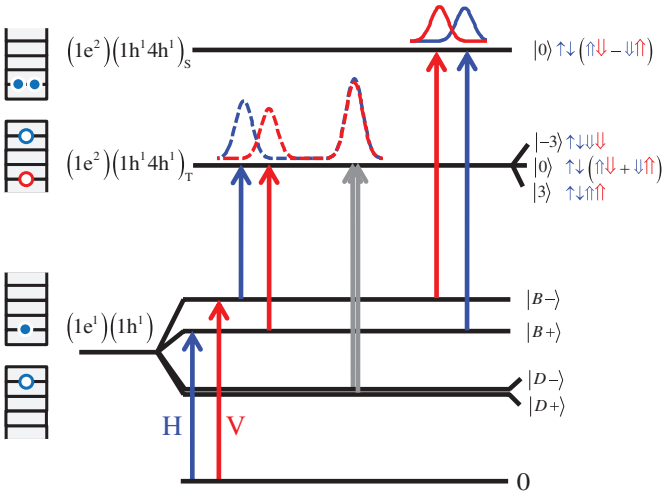

Figure 5. Schematic description of the energy levels and spin wavefunctions of the configuration $|(1e^2)(1h^1 4h^1)\rangle$. The major parts of the spin wavefunctions are presented to the right of each level. The notations are as in figure 4, where ↑(⇓) represents an electron (hole) with spin up (down) and a blue (red) symbol represents a carrier in its first (excited) level. Calculated two-laser PLE spectra are presented by dashed (solid) lines for cross- (co-)linearly polarized excitonic and biexcitonic transitions. Blue (red) lines represent $H(V)$ polarized biexcitonic transitions. Image from [76].

described in this tutorial: the $|(1e^2)(1h^1 4h^1)_{T_0}\rangle$ and the $|(1e^1 1e^2)_{T_{\pm1}}(1h^1 1h^2)_{T_{\mp3}}\rangle$ biexciton states. Figures 5 and 6 display the energy levels of these states. A more detailed description of all of the mentioned biexciton states can be found in Benny *et al* [76].

In principle, the singlet/triplet and singlet/singlet biexcitonic resonances may also occur when the two carriers that form the singlet reside in the same single carrier orbital mode, such that the two carriers are paired. However, due to the small spatial overlap between electron and hole orbital modes belonging to different O numbers, intuitive considerations based on single band models suggest that these transitions should be weak [97]. Specifically, since their dipole moment vanishes, transitions which involve orbital modes of different symmetries should be forbidden. Nevertheless, PLE spectroscopy measurements of quantum wells [98] and QDs [99, 100] have observed some of these forbidden transitions.

In figure 5, we schematically describe the energy levels and the spin wavefunctions of the configuration $|(1e^2)(1h^1 4h^1)\rangle$. The major parts of the spin wavefunctions are displayed to the right of each level, where ↑ (⇓) represents an electron (hole) with spin up (down) and a blue (red) symbol represents a carrier in its first (second) level. The bracketed numbers are the total spin of the configuration. $H(V)$ polarized optical transitions are represented by blue (red) vertical arrows.

The electrons in this configuration are paired in their ground single carrier level, while the holes are unpaired and in different energy levels. One hole is in the $Oh = 1$, s-like, orbital and the other is in the $Oh = 4$, d_{HH}-like orbital. The total spin of the electrons vanishes since the paired electrons form a singlet. Consequently, the degeneracy between the hole triplet states is not removed by the e-h exchange interaction. However, many-carrier mixing effects slightly remove this degeneracy. Our model does not contain anisotropic h–h exchange interactions, to which previous works have attributed this effect [99, 101].

Two absorption resonances are expected from the bright exciton states into an e-singlet/h-singlet biexciton state. These two transitions form a typical cross linearly polarized doublet, similarly to the optical transitions from the vacuum to the bright exciton state. From the exciton states into the three

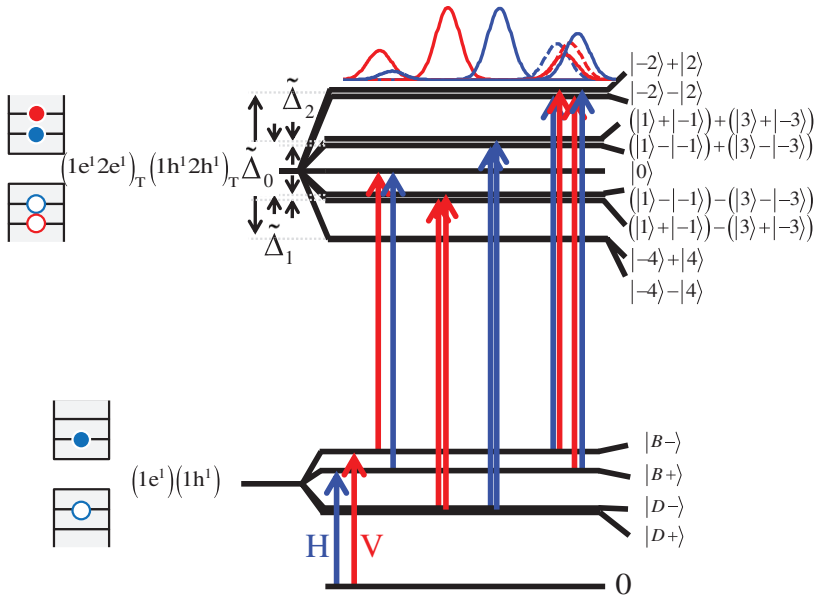

Figure 6. Schematic description of the energy levels of the $|(1e^1 2e^1)_T(1h^1 2h^1)_T\rangle$ biexciton and optical transitions to these energy levels. The major parts of the spin wavefunctions are displayed to the right of each level. A blue (red) vertical arrow represents linearly polarized optical transition along the major (H) (minor (V)) axis of the QD. Image from [76].

e-singlet/*h*-triplet states, four transitions are expected. There will be two cross-linearly polarized transitions from the bright exciton states into the T_0 triplet state with anti-parallel hole spins. There are also two cross-linearly polarized transitions from each of the dark exciton states into the corresponding symmetric and anti-symmetric combinations of the biexciton state with heavy holes in spin triplet states with parallel hole spins, $T_{\pm 3}$. The oscillator strength of the optical transitions from the bright excitonic states is exactly half that of the transitions from the dark exciton states, as can be seen by inspection of the wavefunctions of the initial and final state of each transition. Additionally, the two transitions from the dark excitonic states form one unpolarized spectral line since both the dark exciton and corresponding biexciton pair states are nearly degenerate. Consequently, this spectral line is four times more intense than that of the other two transitions. Figure 5 presents the calculated spectra. To take into the account the finite lifetime of the spin blockaded biexcitons, the calculated transition energies are convoluted with normalized Gaussians of 50 μeV width to obtain the theoretical spectra. Colour is used to represent H (blue) and V (red) linear polarizations. Transitions in which the exciton and biexciton photons are co- (cross-)linearly polarized are presented by solid (dashed) lines.

We now consider optical transitions from the excitonic states into the *e*-triplet/*h*-triplet biexcitonic states. The degeneracy between the states within this subgroup is removed by electron-hole (*e*-*h*) exchange interactions. In the QDs discussed as examples in this tutorial, these interactions are typically about an order of magnitude smaller than the same-carrier exchange interactions. The eigenenergies and eigenstates can be accurately calculated using a CI model [30, 60]. Perhaps more intuitively, an effective biexciton *e*-*h* exchange Hamiltonian for the subspace of $|(1e^1 2e^1)_{T_e}(1h^1 2h^1)_{T_h}\rangle$ can be built using the single exciton effective *e*-*h* exchange Hamiltonian of equation (5), such that an element is defined as follows [102]

$$
\begin{aligned}
{}_f\langle S_z^{(h),2}, S_z^{(h),1}, S_z^{(e),2}, S_z^{(e),1}|H_{XX^0_{1,2,1,2}}|S_z^{(e),1}, S_z^{(e),2}, S_z^{(h),1}, S_z^{(h),2}\rangle_i \\
= {}_f\langle S_z^{(h),1}, S_z^{(e),1}|H_{X^0_{1,1}}|S_z^{(e),1}, S_z^{(h),1}\rangle_i \\
+ {}_f\langle S_z^{(h),2}, S_z^{(e),1}|H_{X^0_{1,2}}|S_z^{(e),1}, S_z^{(h),2}\rangle_i \\
+ {}_f\langle S_z^{(h),1}, S_z^{(e),}2|H_{X^0_{2,1}}|S_z^{(e),2}, S_z^{(h),1}\rangle_i \\
+ {}_f\langle S_z^2, S_z^{(e),2}|H_{X^0_{2,2}}|S_z^{(e),2}, S_z^{(h),2}\rangle_i
\end{aligned}
\tag{10}
$$

where $H_{X^0_{i,j}}$ is the *e*-*h* pair spin Hamiltonian for an electron and hole in the orbital modes i and j respectively, and the subscript i (f) denotes the initial (final) spin state. After transformation to a new basis where the same-carrier exchange states are diagonal, the weak *e*-*h* exchange interactions can then be treated as perturbations on the basis states. Charged excitons (trions) have been described using a similar mathematical approach [103, 104]. If we consider only the subspace of the *e*-triplet/*h*-triplet spin states, $|T_e\rangle \otimes |T_h\rangle$,

$$
\begin{aligned}
|-1,3\rangle &= \downarrow^1\downarrow^2\Uparrow^1\Uparrow^2 && J_z = 2 \\
|-1,0\rangle &= \downarrow^1\downarrow^2 \tfrac{(\Downarrow^1\Uparrow^2+\Uparrow^1\Downarrow^2)}{\sqrt{2}} && J_z = -1 \\
|-1,-3\rangle &= \downarrow^1\downarrow^2\Downarrow^1\Downarrow^2 && J_z = -4 \\
|0,3\rangle &= \tfrac{(\uparrow^1\downarrow^2+\downarrow^1\uparrow^2)}{\sqrt{2}}\ \Uparrow^1\Uparrow^2 && J_z = 3 \\
|0,0\rangle &= \tfrac{(\uparrow^1\downarrow^2+\downarrow^1\uparrow^2)(\Downarrow^1\Uparrow^2+\Uparrow^1\Downarrow^2)}{2} && J_z = 0 \\
|0,-3\rangle &= \tfrac{(\uparrow^1\downarrow^2+\downarrow^1\uparrow^2)}{\sqrt{2}}\ \Downarrow^1\Downarrow^2 && J_z = -3 \\
|1,3\rangle &= \uparrow^1\uparrow^2\Uparrow^1\Uparrow^2 && J_z = 4 \\
|1,0\rangle &= \uparrow^1\uparrow^2 \tfrac{(\Downarrow^1\Uparrow^2+\Uparrow^1\Downarrow^2)}{\sqrt{2}} && J_z = 1 \\
|1,-3\rangle &= \uparrow^1\uparrow^2\Downarrow^1\Downarrow^2 && J_z = -2
\end{aligned}
\tag{11}
$$

the following matrix, neglecting many-body mixing corrections, is obtained:

$$
H_{XX^0_{TT}} = \frac{1}{2}\begin{pmatrix}
\widetilde{\Delta}_0 & 0 & 0 & 0 & \widetilde{\Delta}_1 & 0 & 0 & 0 & 0 \\
0 & 0 & 0 & \widetilde{\Delta}_2 & 0 & \widetilde{\Delta}_1 & 0 & 0 & 0 \\
0 & 0 & -\widetilde{\Delta}_0 & 0 & \widetilde{\Delta}_2 & 0 & 0 & 0 & 0 \\
0 & \widetilde{\Delta}_2 & 0 & 0 & 0 & 0 & 0 & \widetilde{\Delta}_1 & 0 \\
\widetilde{\Delta}_1 & 0 & \widetilde{\Delta}_2 & 0 & 0 & 0 & \widetilde{\Delta}_2 & 0 & \widetilde{\Delta}_1 \\
0 & \widetilde{\Delta}_1 & 0 & 0 & 0 & 0 & 0 & \widetilde{\Delta}_2 & 0 \\
0 & 0 & 0 & 0 & \widetilde{\Delta}_2 & 0 & -\widetilde{\Delta}_0 & 0 & 0 \\
0 & 0 & 0 & \widetilde{\Delta}_1 & 0 & \widetilde{\Delta}_2 & 0 & 0 & 0 \\
0 & 0 & 0 & 0 & \widetilde{\Delta}_1 & 0 & 0 & 0 & \widetilde{\Delta}_0
\end{pmatrix}
\tag{12}
$$

where

$$
\begin{aligned}
\widetilde{\Delta}_0 &= \frac{\Delta_0^{Oe_1,Oh_1} + \Delta_0^{Oe_1,Oh_2} + \Delta_0^{Oe_2,Oh_1} + \Delta_0^{Oe_2,Oh_2}}{4} \\
\widetilde{\Delta}_{1,2} &= \frac{\Delta_{1,2}^{Oe_1,Oh_1} + \Delta_{1,2}^{Oe_1,Oh_2} + \Delta_{1,2}^{Oe_2,Oh_1} + \Delta_{1,2}^{Oe_2,Oh_2}}{8}.
\end{aligned}
\tag{13}
$$

Figure 6 presents the energy levels and spin wavefunctions of the effective Hamiltonian $H_{XX^0_{TT}}$ for the case $\widetilde{\Delta}_2 \ll \widetilde{\Delta}_1 \ll \widetilde{\Delta}_0$. The polarization selection rules of the optical transitions from the ground exciton states are also presented in the figure. Since a photon can carry only a single quanta of angular momentum, biexciton resonances of total spin 0 and 2 can only be reached optically from the bright exciton states. Likewise, biexciton resonances of total spin 1 1 and 3 can be reached only from ground dark exciton states. Biexciton states with a total spin projection of ± 4 are not optically accessible from the exciton.

5.4. Measured PL and PLE spectra of a neutral quantum dot

Figure 7 presents the polarization-sensitive PL spectrum of a single QD in resonance with the microcavity mode. In this case, the QD is a self-assembled InGaAs QD on a GaAs substrate. The QD layer was positioned in the centre of a 1λ microcavity, where the width of the spacer layer approximately corresponds to the wavelength in matter of a photon emitted by the recombination of a ground state exciton. The microcavity is formed by distributed Bragg reflecting (DBR) stacks of alternating $\lambda/4$ layers of AlAs and GaAs. The bottom DBR consists of 25 periods of AlAs/GaAs, and the top reflector has 11 periods of AlAs/GaAs [60, 76].

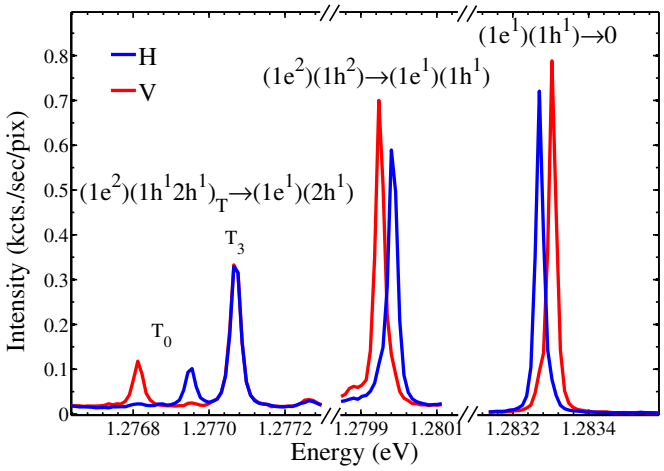

Figure 7. Rectilinear polarization-sensitive PL spectrum, showing the neutral exciton and biexciton lines of a single QD excited by a 501.4 nm CW laser. The corresponding spectral transitions are identified in the figure. Image from [76].

Excitation of the QD with a 501.4 nm CW AR^+ laser was used to obtain the measured spectrum. The QD is, on average, charge neutral at this excitation energy [80]. In order to obtain equal emission intensity from the exciton and biexciton lines, the excitation intensity was roughly 1 $W\,cm^{-2}$ [31]. The corresponding optical transitions are identified above each spectral line in the figure. In addition to the ground bright exciton ($|X^0_{1,1,B\pm}\rangle$) emission lines at $\sim$1.2833 eV and ground biexciton ($|(1e^2)(1h^2)\rangle$ to $|X^0_{1,1,B\pm}\rangle$) lines at $\sim$1.2800 eV, three additional lower-energy biexcitonic lines are observed at $\sim$1.2770 eV. Recombination from the metastable biexciton configurations $|(1e^2)(1h^1 2h^1)_T\rangle$ to excited $|(1e^1)(2h^1)\rangle$ exciton eigenstates accounts for these spectral lines. The two cross-linearly polarized lines at $\sim$1.2769 eV are due to the transitions from the $|(1e^2)(1h^1 2h^1)_{T_0}\rangle$ biexciton configuration to the excited bright exciton eigenstates, $|X^0_{1,2,B\pm}\rangle$. The unpolarized line at $\sim$1.2771 eV is due to the two almost energy-degenerate transitions [85] from the $|(1e^2)(1h^1 2h^1)_{T_{\pm 3}}\rangle$ biexciton configurations to the excited dark exciton configurations, $|X^0_{1,2,D\pm}\rangle$. The observed emission intensity ratio of 1:1:4 corresponds to that discussed previously in section 5.1 [80].

Figure 8 presents the PLE spectra of neutral excitonic and several biexcitonic PL lines. The PL line measured in the corresponding PLE spectrum is indicated by the arrow on the small expanded-scale PL spectra to the left of each graph. Combined with polarization-sensitive PL measurements and the intuition gained from the model outlined in section 5.1, these measurements resulted in the identification of most of the observed one- and two-photon absorption resonances. In the PLE spectral measurements, the identified final states of the optical transitions are marked above the observed transitions.

5.5. Experimental identification of excitonic lines

Figure 8(*a*) displays single photon absorption resonances. The emission from excitonic spectral lines is enhanced upon

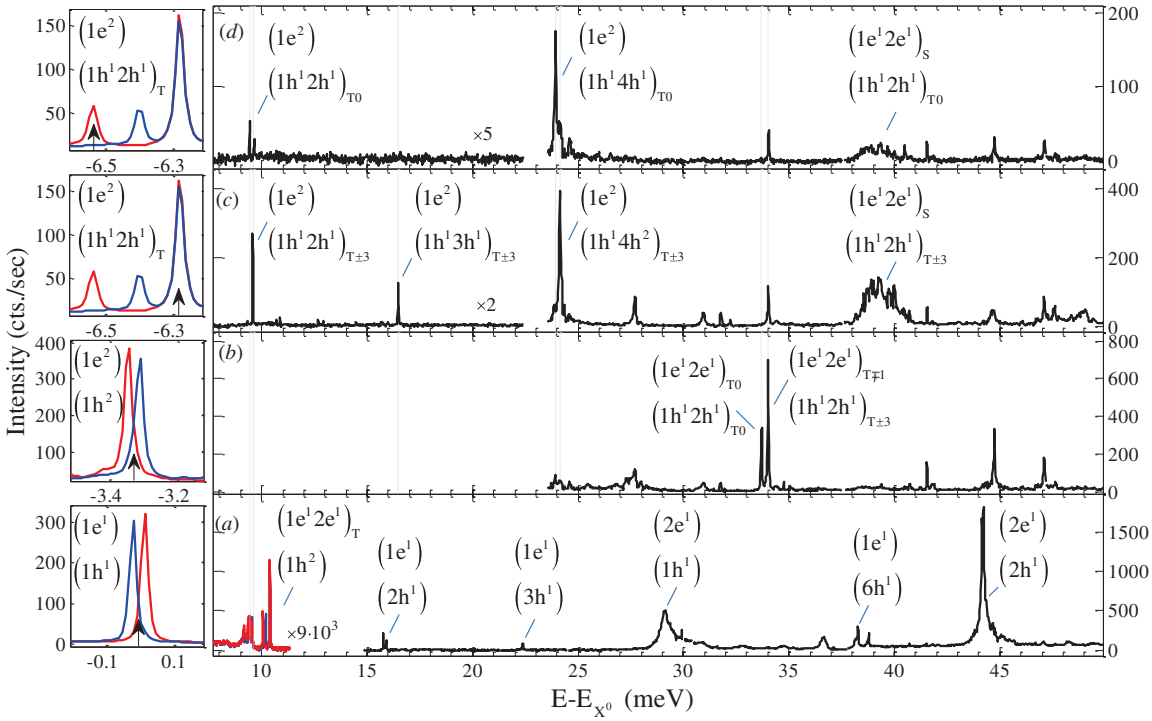

Figure 8. Linearly polarized PL spectra (left panels and the lower energy region in (*a*)) and PLE spectra (right panels) of a single QD. The PLE in (*a*) is measured by a continuous scan of the emission energy of one laser, while a photon detector measured emission from the excitonic emission spectral line. The PLE spectra in (*b*)–(*d*) are measured using two lasers. One laser's emission energy was tuned to the excitonic resonance $(2e^1)(1h^1)$ at 29 meV (as shown in (*a*)), while the energy of the second laser was continuously scanned. The PL line monitored in each case is marked on the corresponding left panel by a vertical black arrow. The assignment of the measured resonances is given by the state to which the QD is excited, and written above each resonance. Image from [76].

resonant absorption of a photon by the empty QD. The $|(2e^2)(2h^2)\rangle$ absorption resonance dominates the spectrum. In this excitonic state, both the electron and the heavy-hole are in their second, p_H-like orbital mode. The large overlap between the orbitals of the two charge carriers accounts for the observed strength of this resonance. Though PLE spectrum contains other sharp absorption resonances, such resonances are weaker by almost an order of magnitude. These resonances correspond to states in which the heavy hole and the electron differ in their orbital mode symmetry, so-called 'non-diagonal' excitonic states. Since the spatial overlap between the modes is small, the oscillator strength of the transition is correspondingly weaker. The $|(1e^1)(6h^1)\rangle$ transition is the highest energy non-diagonal transition which can be identified in this spectrum. Here, the hole is in its d_{VV}-like mode. Since the s-like and d_{VV}-like orbitals are both of even symmetry, there is some amount of overlap which results in a non-vanishing oscillator strength for these transitions [98].

Non-diagonal excitonic transitions between different symmetries, like that to the $|(1e^1)(2h^1)\rangle$ state, are also, somewhat surprisingly, observed. This transition is unambiguously identified by its spectral position and shape, and is the lowest energy resonance in the measured PLE spectrum. It is a cross linearly polarized doublet, with the same energy-order of polarizations and splitting as the ground state excitonic PL line. This is due to optical transitions from the $|(1e^2)(2h^1 1h^1)_{T_0}\rangle$ spin-blockaded biexciton to this, $|(1e^1)(2h^1)\rangle$, excited non-diagonal exciton state (figure 7). In both cases, the same final exciton states dictate the spectral shape. Likewise, the next highest energy order doublet can be identified as corresponding to the non diagonal transitions to the bright levels of the $|(1e^1)(3h^1)\rangle$ exciton. In both of these resonances, $|(1e^1)(2h^1)\rangle$ and $|(1e^1)(3h^1)\rangle$, the electron is excited into its first, s-like, symmetric orbital mode, whereas the hole is excited into the second, p_H-like, and third p_V-like, antisymmetric mode. Since the orbital mode overlap vanishes, these optical transitions are expected to be forbidden. Symmetry breaking, possibly resulting from mixing with other bands, could account for the observation of these transitions [99, 100].

Phonon-induced mixing is another important mechanism permitting symmetry-forbidden transitions. When the phonon energy is resonant with the single-carrier energy level separation, this mixing is particularly strong [105]. The spectrally broad resonance 29 meV above the exciton line shows clear evidence of such mixing-induced excitation. This energy separation corresponds to the energy of LO phonons in GaAs and InAs compounds [106–109]. The $In_xGa_{1-x}As$ optical phonon energy corresponds closely with the $1e$-$2e$ energy level separation, resulting in an enhanced absorption in this spectral domain. The fact that the $|(2e^1)(2h^1)\rangle$ is higher in energy by about 29 meV from the $|(1e^1)(2h^1)\rangle$ resonance also supports this observation.

5.6. Experimental identification of biexcitonic lines

PLE spectra of the various biexcitonic emission lines are presented in figure 8(b)–(d). To perform these measurements, one laser was tuned to the broad excitonic resonance at 29 meV in order to populate the QD with a bright exciton. The emission from the biexcitonic emission lines was then measured as a function of the continuously-varied emission energy of the second laser.

Figure 8(b) presents the PLE spectrum of the ground biexciton doublet, $|(1e^2)(1h^2)\rangle \longrightarrow |(1e^1)(1h^1)\rangle$. The allowed transitions from the bright exciton states of total spin ± 1 into the e-triplet/h-triplet biexcitonic states $|(1e^1 2e^1)_{T_0}(1h^1 2h^1)_{T_0}\rangle$ (total spin zero) and $|(1e^1 2e^1)_{T_{\pm 1}}(1h^1 2h^1)_{T_{\mp 3}}\rangle$ (total spin ± 2) are clearly observed and dominate the measured PLE spectrum.

The PLE measurement of the emission line corresponding to decay of the spin-blockaded metastable biexciton, $|(1e^2)(1h^1 2h^1)_{T_{\pm 3}}\rangle$, is presented in figure 8(c). This emission line corresponds to recombination of the ground e-h pair, resulting in the excited dark exciton states, $|X^0_{1,2,D\pm}\rangle$. The e-triplet/h-triplet resonances dominate this spectrum, which is unsurprising due to the h-triplet of the monitored emission line. The lowest energy resonance in this PLE spectrum corresponds to the absorption resonance transition from the ground state dark exciton $|X^0_{1,1,D\pm}\rangle$ directly to the monitored resonance, $|(1e^2)(1h^1 2h^1)_{T_{\pm 3}}\rangle$, by photogeneration of an $Oe = 1$ $Oh = 2$ e-h pair. Resonances in which the hole is excited into the $Oh = 3$ and $Oh = 4$ orbitals are also clearly identifiable. Photogenerated holes in these resonances relax nonradiatively to the $Oh = 2$ level. Since further non-radiative relaxation is spin-blockaded, this is where recombination occurs [79, 80].

A broad resonance is observed ~29 meV above the $|(1e^2)(1h^1 2h^1)_{T_{\pm 3}}\rangle$ biexciton resonance. This resonance is due to absorption into the $|(1e^1 2e^1)_S(1h^1 2h^1)_{T_{\pm 3}}\rangle$. One LO phonon strongly couples this state to the $|(1e^2)(1h^1 2h^1)_{T_{\pm 3}}\rangle$ state, analogously to the coupling between the $|(2e^1)(1h^1)\rangle$ and the $|(1e^1)(1h^1)\rangle$ states of the bright exciton that was observed in figure 8(a).

Figure 8(d) presents PLE measurements of the metastable biexciton $|(1e^2)(1h^1 2h^1)_{T_0}\rangle$ to the excited bright exciton state $|X^0_{1,2,B+}\rangle$. Similar features are observed. The absorption resonances from the bright exciton states to the $|(1e^2)(1h^1 2h^1)_{T_0}\rangle$ and the $|(1e^2)(1h^1 4h^1)_{T_0}\rangle$ states are identified in this spectrum. Missing from this spectrum due to poor signal-to-noise ratio is the weaker resonant absorption into the $|(1e^2)(1h^1 3h^1)_{T_0}\rangle$ state.

The energy difference between the optical transitions $|(1e^1)(1h^1)\rangle \longrightarrow |(1e^2)(1h^1 2h^1)_{T_0}\rangle$ and $|(1e^2)(1h^1 2h^1)_{T_0}\rangle \longrightarrow |(1e^1)(1h^1)\rangle$ is 15.7 meV. This difference exactly matches the energy of the optical transition from the vacuum into the first excited exciton state, $|(1e^1)(2h^1)\rangle$, as expected.

Absent from the PLE spectrum of the ground biexciton (figure 8(b)) are the transitions to the states $|(1e^2)(1h^1 2h^1)_{T_m}\rangle$ which were clearly observed in figures 8(c) and (d). In the latter cases, the emitting state is directly excited and no intermediate non-radiative relaxation process is necessary. However, when the $|(1e^2)(1h^1 4h^1)_{T_0}\rangle$ state is excited, it is not the case that the emitting state is directly excited. Here, non-radiative relaxation of the hole must occur prior to optical recombination. Consequently, this absorption resonance is observed in the PLE spectrum of the ground biexciton state

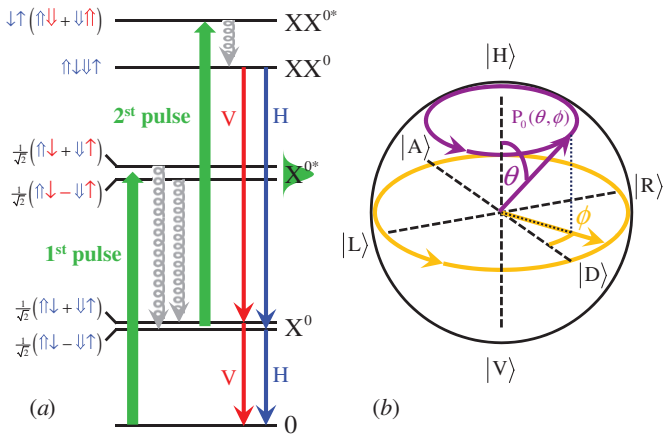

Figure 9. (*a*) A schematic description of writing and reading the exciton spin state. Horizontal lines describe the relative energies of the states, and the spin wavefunctions are provided to the left of the corresponding line. ↑ (⇓) represents a spin up (down) electron (hole). Blue (red) symbols are used to represent a carrier in the ground (excited) energy state. Resonantly tuned light pulses are denoted by green arrows. The first pulse is tuned to an excited exciton state, and the second pulse is tuned to an excited biexciton state. Non-radiative relaxation is indicated by curly lines. Blue (red) lines indicate radiative $H(V)$ polarized recombination. The linewidth of the laser pulses is indicated by a schematic drawing of the pulse spectrum to the right of the energy level diagram, next to the marker for the X^{0*} state. (*b*) The initialization of an exciton spin state with a polarized laser pulse is illustrated on the Bloch sphere. The point $P_0(\theta, \phi)$ represents a spin state of arbitrary polarization. State precession after initialization is indicated by a circle. Image from [57].

as well, suggesting that the hole spin may slightly scatter in the relaxation from the $OH = 4$ to the $Oh = 2$ orbital state [79]. Finally, the resonances $|(1e^12e^1)_{T_{\pm1}}(1h^12h^1)_{T_{\mp3}}\rangle$ and $|(1e^12e^1)_{T_0}(1h^12h^1)_{T_0}\rangle$, corresponding to optical transitions from the bright exciton states, are only observed in the PLE spectrum of the ground biexciton emission line (figure 8(*b*)). Similarly, the resonances $|(1e^12e^1)_{T_{\pm1}}(1h^12h^1)_{T_0}\rangle$ and the $|(1e^12e^1)_{T_0}(1h^12h^1)_{T_{\pm3}}\rangle$, due to optical transitions from the dark exciton states, are observed only in PLE spectra of the spin blockaded biexcitons (figures 8(*c*) and (*d*)). Due to the spectral overlap of the bright exciton resonances $|(1e^12e^1)_{T_{\pm1}}(1h^12h^1)_{T_{\mp3}}\rangle$ and the dark exciton resonances $|(1e^12e^1)_{T_{\pm1}}(1h^12h^1)_{T_0}\rangle$ and $|(1e^12e^1)_{T_0}(1h^12h^1)_{T_{\pm3}}\rangle$, the final identification of these resonances was based on time-resolved and polarization-sensitive spectroscopy [76].

6. Writing and reading the exciton spin configuration

A single, polarized, resonantly-tuned, picosecond light pulse can be used to initialize the exciton spin state in any coherent superposition of its eigenstates. Likewise, a second, delayed picosecond laser pulse, tuned to a biexcitonic absorption resonance and of a given polarization, can be used to project, or 'read out' the spin state of this initialized exciton onto given polarization direction. Figure 9(*a*) is an energy level diagram schematically describing the exciton spin state reading and writing process. To photogenerate an exciton, the first polarized laser pulse is resonantly tuned to an absorption resonance corresponding to an excited exciton state. From this excited state, the exciton rapidly relaxes to its ground state via a non-radiative, spin-preserving process [79, 80].

We will now discuss why the polarization of the light in the exciting laser pulse is related to the spin state of the photogenerated exciton. First, in the direction of propagation, the angular momentum projection of right- (left-) hand circularly polarized light, $R(L)$ is 1 (-1). When such a right- (left-) hand circularly polarized photon generates an *e–h* pair, the electron spin is oriented downward (upward) while the heavy hole spin is pointing upward (downward) in order to conserve the total angular momentum. The spin state of such a pair can be associated with the polarization of the light by the definition $|R\rangle = \Uparrow\downarrow$ ($|L\rangle = \Downarrow\uparrow$). This notation enables a straightforward expression of the correspondence between horizontal (H), vertical (V), diagonal (D), and anti-diagonal (B) linear polarizations of the excitation laser light and the spin state of the photogenerated *e-h* pair:

$$|H\rangle = \frac{1}{\sqrt{2}}(\Uparrow\downarrow + \Downarrow\uparrow) \qquad |V\rangle = \frac{-i}{\sqrt{2}}(\Uparrow\downarrow - \Downarrow\uparrow)$$
$$|D\rangle = \frac{e^{-i\pi/4}}{\sqrt{2}}(\Uparrow\downarrow + i\Downarrow\uparrow) \quad |B\rangle = \frac{e^{i\pi/4}}{\sqrt{2}}(\Uparrow\downarrow - i\Downarrow\uparrow). \qquad (14)$$

Figure 9(*b*) describes these spin states on the Bloch sphere for the exciton spin.

The Poincaré sphere can be used to describe arbitrarily elliptically-polarized pulses. The polarization of such a pulse is represented by a point on the surface of the Poincaré sphere. The coordinates of this point have two components. The D and R directions are contained in the component on the equatorial plane, deflected by an angle ϕ from D. There is also a component parallel to the H–V axis. Therefore, only two angles are necessary to completely define an arbitrary elliptical polarization—the angle ϕ and the angle θ between the polarization and the H–V axis. An arbitrary exciton spin state can be analogously described as a point on the surface of a Bloch sphere. In this case, the north and the south poles of the Bloch sphere are the non-degenerate symmetric and antisymmetric eigenstates of the exciton spin, $|H\rangle$ and $|V\rangle$.

The exciton can be photogenerated in its symmetric (antisymmetric) spin eigenstate $|H\rangle$ ($|V\rangle$) by a resonantly tuned $H(V)$ polarized laser pulse. Since, in this experiment, the 'write' pulse was resonant to an excited exciton state, the photogenerated exciton must relax nonradiatively into its ground state before recombination occurs. The exciton then remains in the corresponding eigenstate until it radiatively recombines. The two spin eigenstates $|H\rangle$ and $|V\rangle$ are non-degenerate–they evolve at different rates. Consequently, a coherent superposition of these eigenstates precesses in time, with the precession frequency given by the difference between the eigenenergies, divided by the Planck constant. Excitation in such a coherent superposition of spin eigenstates requires a resonant pulse whose spectral width contains both eigenenergies. In the time domain, this corresponds to a laser pulse that is much shorter than the precession period. In figure 9(*b*), the orange circle on the equator describes the evolution of an exciton excited by a resonant L-polarized pulse.

This pulse initiates the exciton in a superposition of the $|H\rangle$ and $|V\rangle$ eigenstates with equal probabilities. The initiated spin then precesses counter-clockwise. The spin state becomes, in order, $|D\rangle$, $|R\rangle$, $|A\rangle$ and $|L\rangle$ again after 1/4, 1/2, 3/4 and 1 period. The precession of an exciton spin photogenerated with a pulse of arbitrary polarization $P_0(\theta, \phi)$ is represented by a purple circle.

To verify the polarization of the initialized exciton state, a second polarized pulse is applied with a delay of $\Delta\tau$ from the first pulse. This pulse is tuned to an excited resonance of the biexciton. The probability of photogenerating a biexciton depends on the orientation of the exciton spin state relative to the second pulse polarization. Just like the excited excitonic state, the excited biexciton relaxes nonradiatively into its ground state. Monitoring the dependence of the PL from the ground state biexciton as a function of $\Delta\tau$ yields direct information on the evolution of the spin state of the exciton. It is worth noting here that both the writing of the exciton state and its spin projection read-out are single-shot experiments. That is, if a π-pulse is used to photogenerate the exciton, every laser pulse will result in an exciton with a well-defined spin polarization state, depending on the polarization of the optical pulse. Likewise, if a π-pulse is used to project the exciton spin state or to read it out, it is a single shot operation. This being said, in the actual experimental demonstrations we rely on the detection of an emitted photon from the QD, and temporal averaging over many pulses is required. This is because the efficiency of light harvesting from single QDs is typically limited to a fraction of a per cent. This impediment can in principle be overcome either by increasing light harvesting efficiency [110] or by using photocurrent spectroscopy to read the signal [111, 112].

The 'writing' and 'reading' process which we have described here is not restricted to any specific resonance of the exciton and the biexciton. Phonon-induced mixing is very strong if the single carrier energy level separation [113] resonates with a phonon energy. In this situation, symmetry-forbidden transitions are allowed, and the rate at which the excited state relaxes to the ground state is enhanced. Writing with polarization can also be performed under resonant excitation of the ground state exciton. Larger fidelity of the initialized state is expected in cases where the exciton spin state is directly written.

7. Optically induced rotation of the exciton spin

The technique used for verifying the exciton spin state after initialization, namely transfer of one of the exciton eigenstate populations to an associated biexcitonic state, can also be used to rotate the exciton spin state. The polarized, picosecond, biexcitonic read-out pulse discussed in section 6 selectively couples one of the exciton spin states, while leaving the other state unaffected. The effect of this coupling is a control over the spin state of the exciton manifested as a rotation of the exciton spin on the Bloch sphere about an axis determined by the pulse polarization, by an angle which depends on the pulse detuning. The duration of the pulse is two orders of magnitude shorter than the exciton lifetime (~1 nsec), permitting many

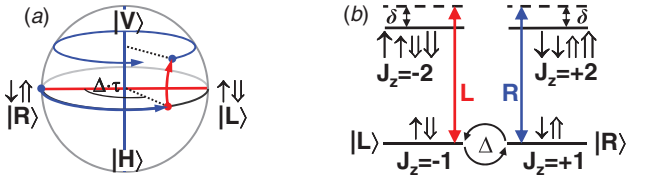

Figure 10. (*a*) The exciton spin state represented on a Bloch sphere. At $t = \tau$, an *R*-polarized biexciton pulse is applied. The circle along (on top of) the equator describes the precession of an exciton spin initialized at $t = 0$ by an *R*-polarized pulse, for $t < \tau$ ($t > \tau$). (*b*) The relevant exciton and biexciton energy levels and the polarization selection rules for a control laser resonant to an excited biexciton transition. The symbol ↑ (⇓) represents an electron (heavy hole) with *z*-direction spin projection $\frac{1}{2}$ ($-\frac{3}{2}$). Short (long) symbols represent charge carriers in their ground (first excited) state. Image from [58].

coherent operations. Methods recently used on ensembles of charged QDs [50, 114] are conceptually similar.

This control experiment begins when the exciton spin wavefunction is written by a *R*- or *L*-circularly polarized laser pulse into the corresponding $|R\rangle$ or $|L\rangle$ spin state. As discussed in section 5.1, the spin precesses in time between the $|R\rangle$ and $|L\rangle$ states [57, 115–117] (figure 10(*a*)). *R*-polarized resonant excitation yields the spin state wavefunction

$$\psi_i(t) = \frac{1}{\sqrt{2}}(e^{i\Delta\cdot t}|H\rangle + i|V\rangle) = a|L\rangle + b|R\rangle$$
$$a = ie^{i\Delta\cdot t/2}\sin(\Delta\cdot t/2);\ b = e^{i\Delta\cdot t/2}\cos(\Delta\cdot t/2) \qquad (15)$$

where $\hbar\Delta$ is the energy difference between the exciton eigenstates. The sample is then excited with a second, delayed, circularly polarized pulse tuned into (or slightly detuned from) an excited biexciton resonance. For this particular control scheme, the $|(1e^1 1e^2)_{T_{\pm 1}}(1h^1 1h^2)_{T_{\mp 3}}\rangle$ biexciton resonance is used (figure 6). However, as the physical phenomena are general, this scheme can be applied to any excited state resonance. This particular resonant level includes two states where the electron spins are parallel each other and antiparallel to the two hole spins. Figure 10(*b*) schematically illustrates these two biexcitonic states. The total angular momentum projection of these states is $J_z = \pm 2$.

The *R* (*L*) polarized pulse carries with it angular momentum of 1 (−1). Consequently, this pulse can couple only the $J_z = 1$ (−1) exciton state to the $J_z = 2$ (−2) biexciton state. The laser pulse duration is much shorter than the exciton precession period. Consequently, the coupled exciton-biexciton states can be safely viewed as an isolated two-level system during the pulse [48]. This system has been solved analytically for the case of a hyperbolic-secant pulse shape [48, 118, 119]. The laser-induced coupling between relevant exciton and biexciton states is given by [119], $C(t) = -\hbar\Omega\cdot\mathrm{sech}(\sigma t)e^{-i\omega t}$, where ω is the laser frequency, σ is the pulse bandwidth, and Ω is the Rabi frequency. When the exciton spin state just before the second pulse is given by (15), the state after an *R*-polarized hyperbolic-secant pulse is thus by [48, 119],

$$\psi_f = a|L\rangle + bF(\alpha, -\alpha, \gamma, 1)|R\rangle$$
$$+ b\frac{i\alpha}{\gamma}F(\alpha+\gamma, -\alpha+\gamma, 1+\gamma, 1)|J_z = 2\rangle \qquad (16)$$

where F is the Gaussian hypergeometric function (also denoted as ${}_2F_1$), and $\alpha = \Omega/\sigma$; $\gamma = \frac{1}{2} - \mathrm{i}\delta/(2\sigma)$, where $\delta = \omega - \omega_0$ is the detuning from resonance frequency ω_0. The probability to populate the biexciton as a function of the time difference τ between the two pulses can then be derived using known properties of hypergeometric functions [119] and is given by

$$P_{XX} = |\langle J_z = 2|\psi_f\rangle|^2 = P^0_{XX}|b(\tau)|^2 = \mathrm{sech}^2\left(\frac{\pi\delta}{2\sigma}\right)\sin^2\left(\frac{\pi\Omega}{\sigma}\right)\cdot\left[\frac{1}{2} + \frac{1}{2}\cos(\Delta\cdot\tau)\right]. \quad (17)$$

From (17), we see that at $\tau = 0$ (i.e. the initialization and control pulses are coincident in time), a non-detuned ($\delta/\sigma = 0$) π-pulse ($\Omega/\sigma = 0.5$) transfers the entire excitonic population to the biexciton state [48]. However in general, the absorption of the second pulse depends on the precession of the exciton spin relative to the control pulse polarization. This results in oscillations in PL emission from the biexciton spectral line, as described in section 6 and [57]. The second pulse also affects the component of the excitonic population which is not transferred to the biexcitonic state. This circularly polarized control pulse couples only to one component of the exciton spin state, affecting the relative amplitude and phase between the excitonic spin eigenstates. The change in the relative phase induced by the control pulse corresponds to a rotation of the exciton Bloch sphere about the $|R\rangle$–$|L\rangle$ axis. The control-induced change in the relative amplitude can likewise be viewed as a compression of the Bloch sphere from the $|L\rangle$ pole towards the $|R\rangle$ pole. Up to normalization, the exciton state after such a control pulse can be expressed by the first two terms of (16). To measure this changed exciton spin state, the spin direction of the exciton must be measured after the control pulse. Measuring the net polarization of the PL from the excitonic emission lines readily yields the spin projection on the $|H\rangle$–$|V\rangle$ axis of the Bloch sphere.

Figure 10 illustrates this idea schematically on the Bloch sphere. When the exciton spin is oriented along the equator, its projection on the $|H\rangle$–$|V\rangle$ axis is zero. This corresponds to an overall spin state where both eigenstates of the exciton are equally populated. However, if the control pulse forces the exciton spin to move in a trajectory which leaves the equator, the populations of the two exciton eigenstates are no longer equal. After the control pulse, the exciton spin again precesses on the Bloch sphere around the $|H\rangle$–$|V\rangle$ eigenstate axis. However, the population difference in the eigenstates, created during the control pulse, remains constant and nonzero. The exciton spin state now has a nonzero projection on the $|H\rangle$–$|V\rangle$ axis of the Bloch sphere. The exciton PL emission is proportional to the probability of population, and $|H\rangle$ and $|V\rangle$ exciton emission can be differentiated energetically. Thus, variations in the PL from exciton spectral lines can be measured and related to the exciton population. The normalized difference between the emission intensities of the two cross-linearly polarized exciton emission lines directly measures the spin projection on the $|H\rangle$–$|V\rangle$ axis of the Bloch sphere. Since the energy difference between the spectral lines of the two exciton eigenstates is larger than their spectral width, the two emission intensities can be simultaneously measured by placing a circular polarizer in front of a monochromator.

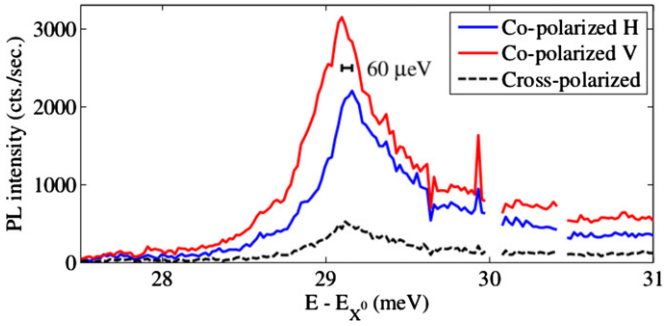

Figure 11. Polarization sensitive PLE spectrum of the $|(2e^1)(1h^1)\rangle$ excitonic resonance. The blue (red) line represent the emission from the bright exciton doublet into the vacuum versus the exciting laser energy, while both the laser and the detection of PL where horizontally (vertically) polarized. The dashed black line represents a measurement where the laser and the PL emission are cross linearly polarized.

In the absence of temporally-resolved PL measurements, the excitonic PL emission will also contain contributions from *incoherent* decay of the biexcitonic population into the excitonic population. However, excitons resulting from incoherent decay of the biexciton equally populate the $|H\rangle$ and $|V\rangle$ eigenstates due to the polarization selection rules (figure 10(*b*)). Thus, decay of the biexcitonic population does not contribute to the difference between excitonic eigenstate populations. Immediately after the control pulse, the population difference can be calculated directly from (16). Using (15) and properties of hypergeometric functions [119] yields,

$$D_{VH} = |\langle V|\psi_f\rangle|^2 - |\langle H|\psi_f\rangle|^2 = -2\mathrm{Re}[a(\tau)\cdot b(\tau)^*\cdot F(\alpha,-\alpha,\gamma,1)^*] = D^0_{VH}\sin(\Delta\cdot\tau) \quad (18)$$

$$D^0_{VH} = \mathrm{Im}\left[\frac{\Gamma^2\left(\frac{1}{2}+\frac{i\delta}{2\sigma}\right)}{\Gamma\left(\frac{1}{2}+\frac{i\delta}{2\sigma}+\frac{\Omega}{\sigma}\right)\Gamma\left(\frac{1}{2}+\frac{i\delta}{2\sigma}-\frac{\Omega}{\sigma}\right)}\right], \quad (19)$$

where $\Gamma(z)$ is the Gamma function. Equation (18) demonstrates that the oscillations in D_{VH} have the same frequency as those of the biexcitonic population, (17). However, they are shifted in phase by $\pi/2$. Equation (19) provides the amplitude of the oscillations and depends on the pulse intensity (Ω/σ) and its detuning normalized by the pulse bandwidth (δ/σ). The sign of the detuning gives the sign of the amplitude, and the amplitude vanishes on resonance ($\delta/\sigma = 0$). From equations (16)–(19), the angle of the induced rotation can be written as

$$\theta = \sin^{-1}\left(D^0_{VH}/\sqrt{1 - P^0_{XX}}\right). \quad (20)$$

7.1. Demonstration of optically induced rotation

Figure 11 presents the polarization sensitive PLE spectrum of the $(2e^1)(1h^1)$ excitonic resonance. The blue (red) line represent the emission from the bright exciton doublet into the vacuum versus the exciting laser energy, while both the laser and the detection of PL where horizontally (vertically) polarized. The dashed black line represents a measurement

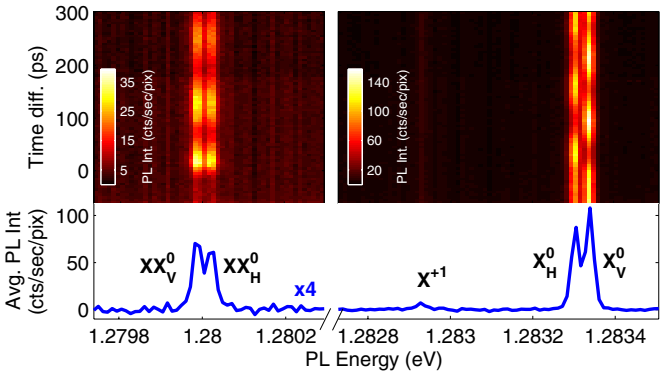

Figure 12. *R*-polarized PL intensity as a function of the photon energy (horizontal axis) and the time difference (vertical axis) between two *R*-polarized laser pulses. The first is tuned into the exciton resonance and initializes the exciton spin state, and the second pulse is detuned by -63 μeV from the biexciton resonance and is used to control the exciton spin state. The temporally averaged spectrum is shown at the bottom. Image from [58].

where the laser and PL emission are cross linearly polarized. As discussed in section 5.5, this resonance is mixed with the ground bright exciton state through induced phonon mixing [105]. The lifetime of this excited state, as judged by its linewidth ($\sim$1 meV), is much shorter than its precession period, as judged by the energy difference between its *H* and *V* co-linearly polarized components (60 μeV—figure 11). The fast relaxation predominantly preserves the initiated spin. Thus, pulsed excitation to that resonance imprints the polarization state of the laser pulse into the spin state of the exciton [57].

Figure 12 presents the *R*-polarized PL intensity (colour) from the QD versus the PL energy (horizontal axis) and the time difference τ (vertical axis) between the initialization and control pulses. The initialization pulse writes the exciton spin–spin state and is tuned to the $|(2e^1)(1h^1)\rangle$ excitonic absorption resonance. The control pulse is detuned by -63 μeV from the $|(1e^12e^1)_{T_{\pm1}}(1h^12h^1)_{T_{\mp3}}\rangle$ biexcitonic resonance (figures 6 and 8). The two lasers are co-circularly *R* polarized. Emission from the ground state biexciton (exciton) is the lower (higher) energy emission line doublet. The precession of the exciton spin state after initialization by the first pulse [57] is reflected in the oscillations of the PL emission from the biexciton, whose intensity reads out the exciton spin state. Equation (17) describes this behaviour. The variations in the exciton spin projection on the eigenstate axis of the Bloch sphere induced by the control pulse, as described by equation (18), are visible as oscillations in the PL from the two excitonic components. Recombination of the positively charged exciton results in the faint spectral line at 1.282 93 eV is due to the positively charged exciton. PL emission from the positively charged exciton does not oscillate with τ.

The angle by which the exciton spin projection is rotated depends on the detuning of the control pulse from resonance. First, the energy of the control laser was varied around the $J_z = \pm2$, $|(1e^12e^1)_{T_{\pm1}}(1h^12h^1)_{T_{\mp3}}\rangle$ absorption resonance for a fixed time difference between initialization and control of 30 ps. The intensity of the second, control, pulse was tuned to slightly below the intensity required for population inversion at resonant excitation, a value chosen in order to observe both exciton and biexciton emission lines during the experiment. Simultaneous observation of exciton and biexciton emission lines allows simultaneous testing of equations (17) and (19). Figure 13(*a*) shows this PLE spectrum of the biexcitonic absorption resonance. The calculated biexciton population (17) for a 9 psec FWHM hyperbolic-secant pulse ($\hbar\sigma$ = 145 μeV) is represented by a dashed line. The measured values deviate from the calculated values at low energies. This deviation is due to a nearby excited biexciton absorption resonance, $J_z = 0$, $|(1e^12e^1)_{T_0}(1h^12h^1)_{T_0}\rangle$. Allowing for this deviation, the width of the $J_z = \pm2$ resonance corresponds well to the calculated theoretical width. The fact that the resonance width is completely determined by the spectral width of the laser indicates that this excited biexciton state does not relax into lower-energy biexciton states during the control pulse. The different spin configuration of these states and the slow spin dephasing rate of the QD-confined charge carriers [46] explain this effect. The resonance width implies that the $J_z = \pm2$ biexciton remains coherent during the entire control pulse.

Figure 13(*b*) presents the biexciton PL intensity as a function of τ. The black (blue) line represents off (almost on) biexcitonic resonant excitation. The dependence on time difference is cosinusoidal in both cases, as seen in equation (17). The intensity of the PL emission from the exciton lines as a function of τ, for the same almost-on- and off-resonant biexcitonic excitation is presented in figure 13(*c*). The solid (dashed) line denotes the PL from the *H*- (*V*-) polarized component of the excitonic emission line doublet. The difference between the PL intensities from these two cross-linearly polarized exciton emission lines, normalized by the sum of their intensities at negative delay time, before the arrival of the control pulse, is presented for a variety of detuning values in figure 13(*d*). As in (18), the oscillations are sinusoidal in τ. The dependence of the amplitude on the detuning is clearly visible. Below resonance, the amplitude is negative. Above resonance, the amplitude is positive. On resonance, the amplitude vanishes, as expected from (19).

Figure 14 summarizes this dependence by displaying the measured excitonic PL oscillation amplitudes as a function of the normalized detuning, δ/σ. The dashed lines present the amplitude calculated by equation (19), for $\Omega/\sigma = 0.35$ (0.7π-pulse), which corresponds well to the control pulse power used in this experiment. Co- (cross-)circularly polarized laser pulses are displayed in blue (red). The inset displays the measured and calculated spin rotation angles from (20) on the same normalized detuning axis.

8. Complete control of the exciton spin by a 2π-area pulse

The realization of quantum information processing requires matter qubits. The spin of a particles is a promising matter qubit candidate, since electronic, nuclear, or atomic spins are natural and relatively protected two-level physical systems. The spin state of these particles can be described as a coherent superposition of the two spin states, and geometrically

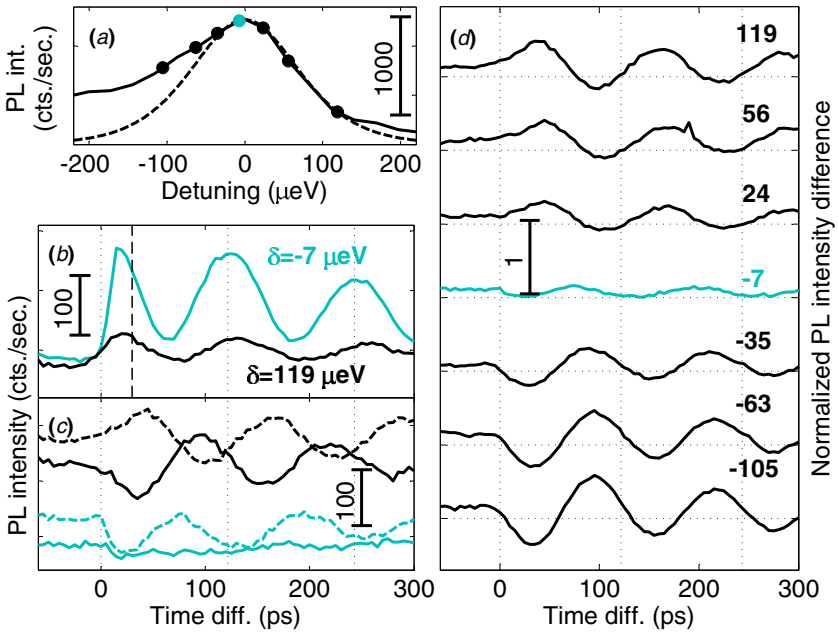

Figure 13. (*a*) The solid line displays the measured biexciton PL intensity versus the control laser detuning from the biexciton absorption resonance at a fixed $\tau = 30$ ps. Circles represent the specific energies used for the measurements presented in (*b*)–(*d*). The dashed line is the calculated P_{XX} (17), for a pulse of 9 ps FWHM ($\hbar\sigma = 145\ \mu$eV). (*b*) Biexciton intensity versus τ close to (light blue) and far from (black) resonance. The vertical dashed line denotes $\tau = 30$ ps. Detuning values are given next to the corresponding curve. (*c*) The solid (dashed) line denotes the PL intensity of the H (V) component of the exciton doublet versus τ, close to and far from resonance, as in (*b*). The curves are vertically shifted for clarity. (*d*) The differences between the PL from the V and H components, normalized by their sum at negative τ, for the energies marked by circles in (*a*) and specified in μeV next to each curve. Vertical dotted lines present integer spin precession periods $T{=}h/(34\ \mu\text{eV}) = 122$ psec. Image from [58].

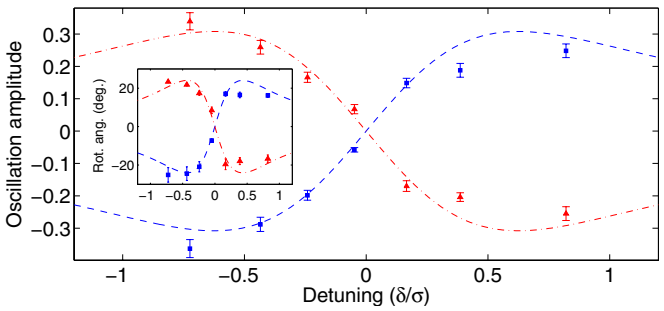

Figure 14. Measured (symbols and error bars obtained by model fitting to the data in figure 13(*d*)) and calculated (dashed line) oscillation amplitudes of the exciton polarization versus the normalized detuning δ/σ, where $\hbar\sigma = 145\ \mu$eV and $\Omega/\sigma = 0.35$ (0.7π-pulse). Blue (red) colour describes co- (cross-)circularly polarized pulses. Inset: the measured and calculated rotation angles for a 0.7π pulse. Image from [58].

represented as a vector from the centre to a point on the surface of a Bloch sphere, a unit sphere whose poles correspond to the two spin eigenstates of the system. For a qubit, the state of the system must be fully controllable. This type of universal operation can be described geometrically as a rotation of the qubit state vector about any desired axis, by any desired angle [7, 8]. These universal operations must be performed with high fidelity, and they must be completed in a short time. The time required by the operation should be shorter than the qubit's life and decoherence times by orders of magnitude [15].

When the two spin eigenstates are not degenerate, such as in the presence of a magnetic field, a state composed of a superposition of these eigenstates will evolve in time. This time evolution can be described geometrically as a precession of the state vector about an axis connecting the poles of the Bloch sphere. The frequency of precession is given by the energy difference between the two eigenstates, divided by the Planck constant.

So far, demonstrated control methods use a sequence of optical pulses to induce fixed rotations of the qubit around axes that differ from the precession axis. Between these pulses, a delay allows for coherent precession of the qubit, thus achieving a universal operation. Clearly, the addition of this fixed delay stage in such a sequence of steps increases the time necessary to perform the operation. This results in an operation time comparable to the precession period. Additionally, the overall fidelity of the operation is the product of the fidelities of each step, such that an operation with more steps will have a lower overall fidelity.

In contrast, we demonstrated [59], that it is possible to achieve complete control of a matter qubit using a single picosecond optical pulse. This qubit was composed of an optically excited electron (exciton) in *a single semiconductor QD* [57, 58, 79, 120–122]. The techniques we used to achieve single-pulse control are not unique to this qubit system. They are generally applicable to other systems as well. This single-pulse control was one of the first demonstrations of a fast and efficient universal single-qubit gate, something which had not been demonstrated previously in other qubit systems.

As a candidate qubit, spins of charge carriers confined in semiconductor QDs are particularly important [22, 123] since they are compatible with current semiconductor technologies

and since they enable an interface between flying qubits such as photons and the anchored spin qubit. Spin control in QDs has already been well-demonstrated, and techniques include radio-frequency pulses [27, 28] and by optical means using stimulated Raman scattering [46, 47, 54] or by accumulation of a geometrical phase through resonant excitation [48–52, 114].

We have discussed previously how an excitonic qubit can be prepared in a given spin state [57] (section 6). The ability to prepare the qubit in a given state enables the next demonstration, that of full control over this state after initialization. The control pulse is a single 2π-area optical pulse, tuned or slightly detuned from a non-degenerate biexciton resonance. The excitonic population is transferred into itself via the 2π-pulse, through a process of photon absorption and stimulated emission. During this pulse, the two eigenstates of the exciton spin acquire a relative phase difference, and it is this phase difference that results in rotation of the exciton spin state. The energy detuning of the control pulse from the biexciton resonance determines the rotation angle, and the polarization of the control pulse determines the spin rotation axis [57, 58]. This process is different from control of a single carrier spin as demonstrated in [27, 28, 46–52, 54, 114] or the process we described previously in [7] and [58] for controlling the exciton spin with a degenerate resonance. In these cases, polarization is used to distinguish between degenerate optical transitions. Consequently, the polarization degree of freedom is lost and only a fixed, *well-defined* rotation axis is present.

We now describe the control of a coherent exciton spin state, which can be described as a vector on the Bloch sphere

$$\begin{aligned}|X(\theta,\phi)\rangle &= \cos\left(\frac{\theta}{2}\right)|H\rangle + \mathrm{i}\mathrm{e}^{\mathrm{i}\phi}\sin\left(\frac{\theta}{2}\right)|V\rangle \\ &= \alpha(\theta)|H\rangle + \beta(\theta,\phi)|V\rangle \end{aligned} \quad (21)$$

where $|H\rangle$ and $|V\rangle$ are the two spin eigenstates $1/\sqrt{2}[(1e^1)_{-1/2}(1h^1)_{3/2} + (1e^1)_{1/2}(1h^1)_{-3/2}]$ and $1/\sqrt{2}[(1e^1)_{-1/2}(1h^1)_{3/2} - (1e^1)_{1/2}(1h^1)_{-3/2}]$ respectively. The poles of the Bloch sphere are these two non-degenerate eigenstates (figure 9). A short optical pulse, resonantly tuned to an excitonic transition and whose bandwidth is larger than the energy splitting between the eigenstates, can generate an exciton in this coherent superposition. The pulse polarization is given by:

$$\vec{P}_X(\theta,\phi) = \cos\left(\frac{\theta}{2}\right)\hat{H} + i\mathrm{e}^{\mathrm{i}\phi}\sin\left(\frac{\theta}{2}\right)\hat{V}, \quad (22)$$

where $\hat{H}$ ($\hat{V}$) represents a linear polarization parallel to the major (minor) axis of the QD [57, 76].

Here, the biexcitonic resonance used for the probe and the control contains two excitons with different spatial symmetries and antiparallel spins. In our notation, this resonance is described as $|(1e^2)(1h^14h^1)_{T_0}\rangle$. The two electrons form a spin singlet in the ground energy state. The holes are in two different energy levels, one in the ground s-like level and one in the d_{HH}-like forth level, and they form a triplet state with zero total spin projection [76] (figure 5). Consequently, a polarized pulse in such a resonance couples exclusively to the exciton with the opposite spin state. This means that an R-polarized pulse couples to $|L\rangle$, D to $|\bar{D}\rangle$, and H to $|V\rangle$, where P is the probe pulse polarization and $|P\rangle$ is the corresponding exciton spin state of the exciton [57]. The absorption is maximized if the polarization of the second pulse is cross-polarized relative to the exciton spin, or with the polarization of the first pulse in the case that the two pulses are simultaneous,

$$\vec{P}_{XX}(\pi-\theta,\pi+\phi) = \sin\left(\frac{\theta}{2}\right)\hat{H} - \mathrm{i}\mathrm{e}^{\mathrm{i}\phi}\cos\left(\frac{\theta}{2}\right)\hat{V}, \quad (23)$$

as described in [57, 76]. The cross-polarized exciton state

$$\begin{aligned}|\bar{X}(\theta,\phi)\rangle &= |X(\pi-\theta,\pi+\phi)\rangle \\ &= \sin\left(\frac{\theta}{2}\right)|H\rangle - \mathrm{i}\mathrm{e}^{\mathrm{i}\phi}\cos\left(\frac{\theta}{2}\right)|V\rangle \\ &= \alpha(\theta)|H\rangle + \beta(\theta,\phi)|V\rangle \end{aligned} \quad (24)$$

is maximally coupled to 'cross polarized' pulses with polarization described by (22), but unaffected by resonant pulses that are 'co-polarized'. Figure 15 illustrates this control scheme.

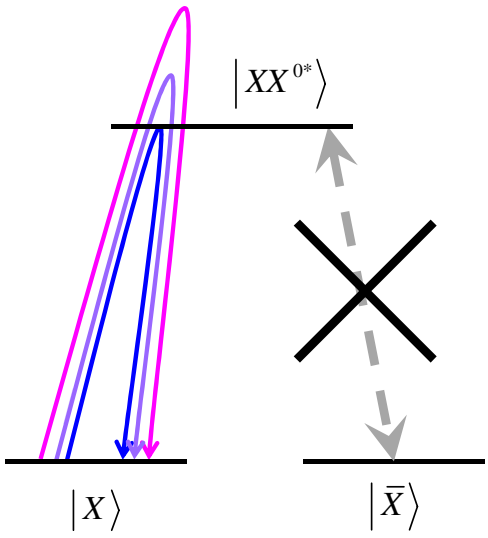

Figure 15. A schematic energy level diagram of the exciton and biexciton states involved in the single-pulse control experiment. Here, $|X\rangle$ ($|\bar{X}\rangle$) is the coupled (uncoupled) state. The $|(1e^2)(1h^14h^1)_{T_0}\rangle$ biexciton state is represented by $|XX^{0*}\rangle$. The curved arrows depict 2π-pulses with different energy detunings. The dashed grey arrow represents the restricted uncoupled transition.

An arbitrary coherent excitonic state such as:

$$\begin{aligned}|X(\theta',\phi')\rangle &= \cos\left(\frac{\theta'}{2}\right)|H\rangle + \mathrm{i}\,\mathrm{e}^{\mathrm{i}\phi'}\sin\left(\frac{\theta'}{2}\right)|V\rangle \\ &= \alpha(\theta')|H\rangle + \beta(\theta',\phi')|V\rangle \end{aligned} \quad (25)$$

can be conveniently expressed also in terms of the coherent states $|X(\theta,\phi)\rangle$ and $|\bar{X}(\theta,\phi)\rangle$ as:

$$|X(\theta',\phi')\rangle = \alpha(\theta^p)|X(\theta,\phi)\rangle + \beta(\theta^p,\phi^p)|\bar{X}(\theta,\phi)\rangle, \quad (26)$$

where spherical symmetry considerations are used, and the angles θ^p and ϕ^p are measured relative to the pulse polarization direction.

The $|\bar{X}(\theta,\phi)\rangle$ part of the exciton wavefunction acquires a geometrical phase relative to the$|X(\theta,\phi)\rangle$ part, since the $\vec{P}_{XX}$ polarized 2π-area pulse couples only to the $|\bar{X}(\theta,\phi)\rangle$

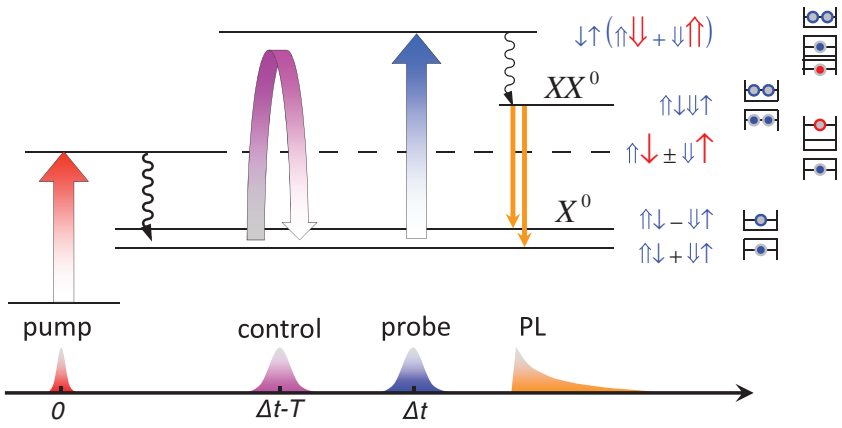

Figure 16. A schematic description of the pulse sequence used for initialization (pump), control and read-out (probe) of an exciton spin state. To the right of each level, the relevant exciton and biexciton levels and corresponding spin wavefunctions are presented. ↑ (⇑) denotes electron (hole) spin state. Short blue (long red) symbols are used to denote the ground (excited) state. Image from [59].

component. This induced phase shift results in a rotation angle that depends on the pulse shape and energy detuning. The phase shift (η) for a hyperbolic secant 2π-pulse of temporal form of $\mathrm{sech}(\sigma \cdot t)\mathrm{e}^{\mathrm{i}(E_0-\delta)t/\hbar}$ is given by

$$\eta = \pi - 2\arctan\left(\frac{\delta}{\sigma}\right) \tag{27}$$

where E_0 is the energy of the biexciton resonance, δ is the detuning of the pulse from resonance, and σ is the pulse bandwidth [48, 49, 58]. After the control 2π-pulse, the new exciton state is

$$\begin{aligned}|X(\theta'', \phi'')\rangle &= \alpha(\theta^p)|X(\theta,\phi)\rangle + \mathrm{e}^{-\mathrm{i}\phi}\beta(\theta^p,\phi^p)|\bar{X}(\theta,\phi)\rangle \\ &= \alpha(\theta^p)|X(\theta,\phi)\rangle + \beta(\theta^p,\phi^p-\eta)|\bar{X}(\theta,\phi)\rangle.\end{aligned} \tag{28}$$

Geometrically, the control pulse action can be described as a clockwise rotation by an angle η about an axis connecting the states $|X(\theta,\phi)\rangle$ and $|\bar{X}(\theta,\phi)\rangle$, which is parallel to the control pulse polarization direction.

It then follows that during a pulse that is exactly resonant relative to the uncoupled state, the coupled part of the state acquires a relative geometric phase shift of π radians, a semicircle on the Bloch sphere [48, 49]. Continuing with the Bloch sphere depiction, this relative phase acquisition can be viewed as a clockwise π rotation of the state vector about an axis which is defined by the polarization direction of the control pulse [48, 49, 58]. Angles of rotation differing from π can be achieved by detuning from resonance [48, 49, 58]. These controls over angle and direction create a universal gate operation from a *single* light pulse.

To describe the control action, we begin with a unit vector in the exciton polarization direction $|X(\theta,\phi)\rangle$. This state couples to a polarized 2π control pulse as:

$$\hat{n} = (n_x, n_y, n_z) = (\cos\phi\sin\theta, \sin\phi\sin\theta, \cos\theta) \tag{29}$$

where we choose the Cartesian axes such that: $\hat{x} \equiv |R\rangle = 1/\sqrt{2}(|H\rangle + \mathrm{i}|V\rangle)$, $\hat{y} \equiv |\bar{D}\rangle = 1/\sqrt{2}(|H\rangle - \mathrm{i}|V\rangle)$, $\hat{z} \equiv |H\rangle$. As discussed previously, the control pulse essentially rotates the exciton wavefunction about $\hat{n}$ by the angle η. In the eigenstate basis, such a rotation is described by the operator:

$$R_{\hat{n}}(\eta) = \exp\left(\mathrm{i}\vec{\sigma}\cdot\hat{n}\frac{\eta}{2}\right), \tag{30}$$

where $\vec{\sigma} \equiv (\sigma_x, \sigma_y, \sigma_z)$ is the vector of Pauli spin matrices. Applying this operator to an exciton state such as $|X(\theta',\phi')\rangle$ (equation (28)), the freedom in choosing ϕ, η and θ enables a universal rotation of the exciton spin polarization.

8.1. Experimental demonstration of single-pulse complete control

This single pulse control can be demonstrated experimentally using a synchronized sequence of three optical pulses. Figure 16 depicts the control sequence. The first optical pulse is a polarized pulse tuned to the $(2e^1)(1h^1)$ exciton absorption resonance, which was described in figure 11. This pulse photogenerates an exciton. The polarization of the laser pulse translates into exciton spin polarization with high fidelity [57].

Another picosecond pulse, tuned into the $|(1e^2)(1h^1 4h^1)_{T_0}\rangle$ biexciton resonance [57], is used to probe (read) the exciton spin state (figure 5). This pulse transfers the excitonic population into a biexcitonic population by photogenerating an additional electron-hole pair in the QD [57, 58, 76]. As was previously explained, the absorption of this probe pulse is dependent on the relative spin orientation of the two electron-hole pairs. The spin of the second pair is defined by the probe pulse polarization, and consequently, absorption of the probe pulse measures the spin projection of the initial exciton on the probe polarization direction [57, 58, 76]. The magnitude of the probe pulse absorption can be directly deduced from the PL intensity of the biexciton emission lines [76].

Figure 16 schematically describes the experiment and depicts the relevant energy levels, the resonant optical transitions between these levels, and the sequence of the laser pulses. PL and PLE spectroscopy of the QD with one and two resonant lasers [76], results of which are presented in figure 8, were used to identify the absorption resonances used in this

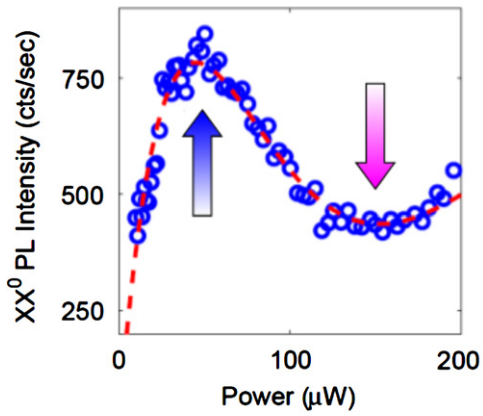

Figure 17. The biexciton PL intensity versus the probe pulsed laser power tuned to the biexcitonic resonance, $|(1e^2)(1h^1 4h^1)_{T_0}\rangle$, 60 psec after a resonant laser pulse to the $(2e^1)(1h^1)$. The vertical blue and magenta arrows indicate the laser power which corresponds to pulse area of π (used for the probe) and 2π (used for the control) pulses, respectively. The dashed line guides the eye. Image from [59].

experiment. Figure 17 presents the dependence of biexciton PL emission intensity on the power of the excitation laser tuned to the selected biexciton resonance. Rabi oscillations are clearly visible, and the intensities corresponding to a π pulse (probe) and 2π-pulse (control) are indicated with arrows.

Figure 18(a) schematically illustrates optical control on the exciton spin Bloch sphere. The precession of the exciton spin after initialization by an L-polarized pulse (thick red arrow) is represented by a red circle. The direction of the polarization of the control 2π pulse is described by the thick magenta arrow in figure 18(a). The rotation of the exciton state during the control pulse is represented likewise by a dashed magenta line. The solid blue line describes the new precession of the exciton spin state *after* the end of the control pulse. In figure 18(b), the red solid line illustrates the measured biexciton PL emission as dependent on the delay time between the pump and the L polarized probe pulse for an $|L\rangle$ initiated exciton (Δt). In contrast, the blue curve represents the measured biexciton PL emission versus the time difference Δt between the pump and probe pulses. However, in this case, a control pulse is applied exactly one precession period *before* the probe pulse. Thus, the control action is detected a period after it occurs. The control pulse changes the phase of the oscillation relative to the experiment in the absence of a control pulse.

In figures 19–20 we display three series of experiments which demonstrate our ability to perform universal gate operations on the exciton state using a *single* optical pulse. In these experiments, like in figure 18, the exciton is always photogenerated in its $|L\rangle$ coherent state by an L polarized pulse. The probe pulse, which in these experiments is delayed continuously relative to the pump, is also L polarized, thus projecting the exciton state onto the $|R\rangle$ state. The lowest, black solid line in each figure describes for comparison the two-pulse experiment in the absence of a control pulse, in which the precession of an $|L\rangle$ photogenerated exciton is probed by the delayed L-polarized probe pulse [57].

The control 2π-pulse in these experiments is always applied one precession period (T = 122 psec) *before* the probe pulse. This means that for Δt less than the precession period, the control pulse arrives before the pump pulse and no exciton is present in the QD in these cases. Consequently, when $\Delta t < T$, the observed biexciton emission resembles that visible in the case of no control pulse. However for $\Delta t > T$, the control pulse arrives after the pump pulse, and its effect on the phase of the biexciton emission signal is clearly visible.

The first two sets of experiments are presented in figure 19. Here, the control pulse is tuned to resonance. Its polarization is given by $\vec{P}(\theta, \phi) = \vec{P}(\pi/2, \pi + \alpha)$ in figure 19(a) and $\vec{P}(\theta, \phi) = \vec{P}(\pi/2 + \alpha, \pi)$ in figure 19(b). The angle α spans seven equally spaced values from 0 (L polarization) to $\pi/2$, corresponding to D polarization in (a) and V polarization in (b). The values of α are provided to the left of each curve. The Bloch spheres to the left of figures 19(a) and (b) describe the rotation schematically. The control pulse rotates the exciton state vector around the polarization direction $\vec{P}$ by an angle π. The depicted Bloch sphere trajectory (dashed line) represents this control rotation as applied to the initial $|L\rangle$ state. In

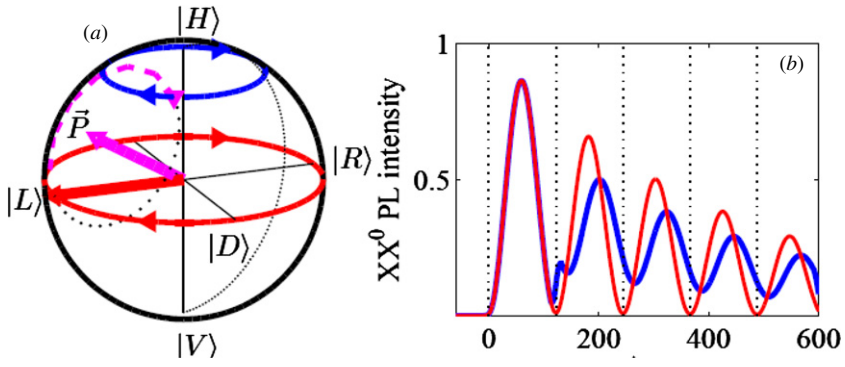

Figure 18. (a) The red circle represents precession of the exciton spin after photogeneration by an L polarized pump pulse. The polarization of the control pulse is represented by the magenta arrow. The dashed magenta trajectory represents the rotation of an $|L\rangle$ exciton state about the polarization direction, imposed by the control pulse. The blue line represents the precession of the spin after the control pulse. (b) The biexciton PL intensity (orange arrows in figure 16) as a function of the delay time (Δt) between the pump (red arrow in figure 16) and probe (blue arrow in figure 16) pulses. The red line depicts initialization with an L polarized pulse and probing with an L polarized pulse. The blue trace, in contrast, represents the signal where the control pulse, polarized as shown in (a), is applied one period (T = 122 psec) before the probe pulse. Note that the control pulse changes the phase of the oscillation relative to the two-pulse experiment. Image from [59].

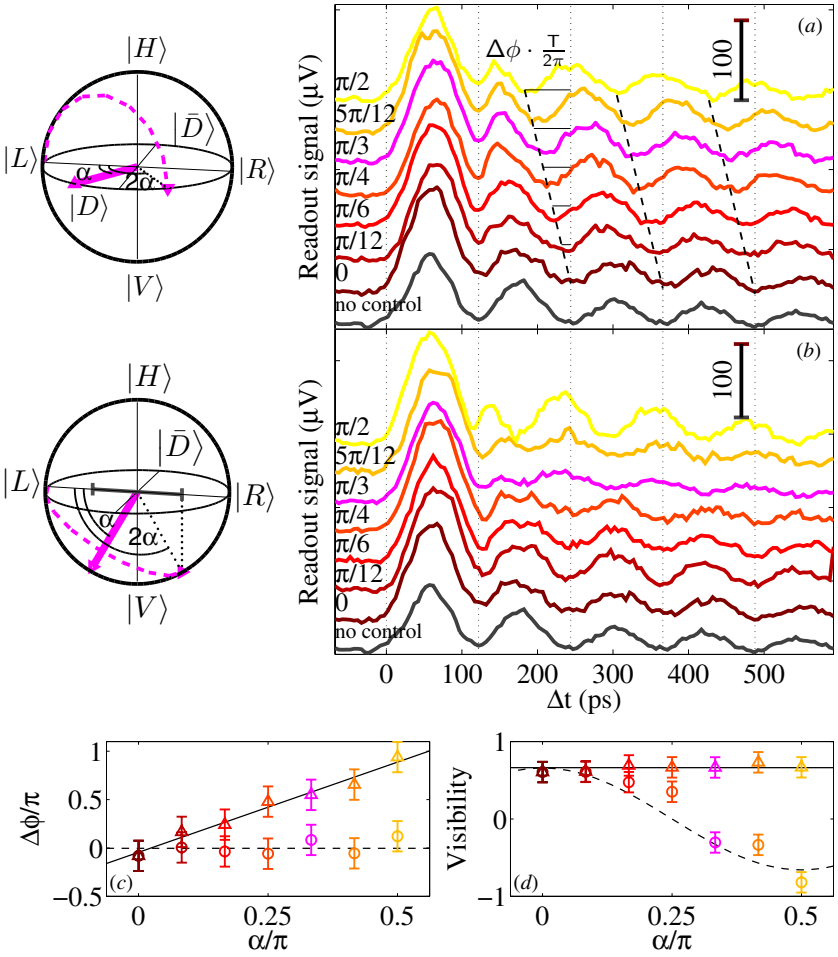

Figure 19. Experimental measurements of biexciton PL intensity (lock-in detected with the probe laser pulse) versus Δt for various control pulse polarizations given by (*a*) $\vec{P}(\theta,\phi)=\vec{P}(\frac{\pi}{2},\pi+\alpha)$ and (*b*) $\vec{P}(\theta,\phi)=\vec{P}(\frac{\pi}{2}+\alpha,\pi)$. α varies from $\alpha=0$ (L polarization) to $\alpha=\pi/2$ (D polarization in (*a*) and V polarization in (*b*)). The control pulse is applied one period of oscillation before the probe. The lowest, black curve in (*a*) and in (*b*) describes the measurement without the control pulse and is used for normalization. The Bloch spheres to the left of each panel schematically describe the rotation of the exciton spin state induced by the polarized control pulse. The arrow represents control pulse polarization direction and the dashed line is the exciton spin state trajectory. (c) (d) Symbols represent the phase shifts (normalized visibilities) of the exciton spin precession induced by the control pulse versus α. The circle (triangle) colouring corresponds to the colours in (*a*) (*b*). The black solid (dashed) lines are best fits to the experimental points in (*a*) (*b*). Image from [59].

figure 19(*a*) the rotation always leaves the exciton state on the equator plane, but adds a phase shift corresponding to twice the angle α. In contrast, in figure 19(*b*) the rotations leave the exciton phase unchanged but varying the state projection on the equator, or visibility, as $\cos(2\alpha)$.

Figure 19(*c*) displays the measured phase shift of the exciton state and figure 19(*d*) displays its projection on the Bloch sphere equator, or visibility, as a function of α for both of the control pulse schemes presented in parts (*a*) and (*b*) of the same figure. As expected from the Bloch sphere description of the effect of the control pulse, the visibility does not vary for the rotation scheme in (*a*) while the phase shift varies linearly, increasing from 0 to π as alpha varies from 0 to $\pi/2$. Solid lines describe the best fits for this control pulse sequence. Likewise, for the control scheme in (*b*), the visibility varies as $\cos(2\alpha)$ while the phase is unaffected. The best fits to this control pulse sequence are presented by dashed lines.

The demonstration of single pulse control is completed by showing the effect of pulse detuning from the resonance energy. Figure 20(*a*) presents a series of measurements of fixed control pulse polarization corresponding to $\vec{P}(\theta,\phi)=\vec{P}(\pi,\pi)$ (V polarization). The pulse detuning from resonance is varied. The situation is schematically described on the Bloch sphere on the left of figure 20(*a*) to demonstrate the rotations of the exciton state by the control pulse. In this case, rotation is achieved through variation in the angle by which the control pulse rotates the state around the polarization direction. The exciton state remains on the equator, as shown in the figure. The control pulse adds an additional phase of η (equation (27)) to the exciton state azimuthal angle ϕ. Figure 20(*c*) presents the measured phase shift and figure 20(*d*) the visibility of the biexciton PL emission as functions of the detuning δ in units of the laser bandwidth σ. As expected, the visibility does not vary with the detuning, while η varies from $\sim 3\pi/2$ to $\pi/2$ as δ/σ varies from -1 to 1.

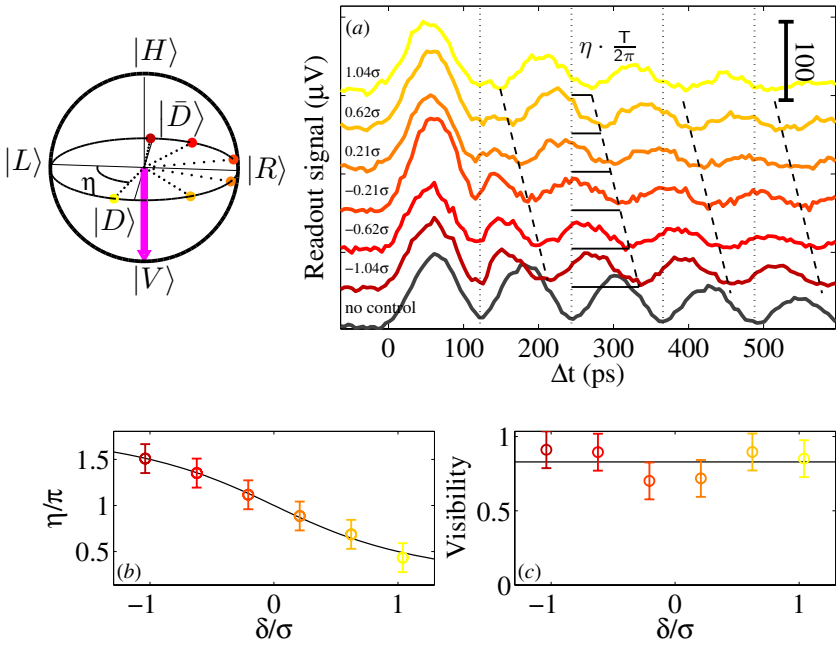

Figure 20. (*a*) Biexciton PL intensity versus Δt for a V polarized variably detuned control pulse. The control pulse induces a rotation of the exciton spin state, which is schematically described as a trajectory on the Bloch sphere to the left of the graph. (*b*) (*c*) Circles: the phase shifts (normalized visibilities) of the exciton spin versus the detuning δ in units of the pulse bandwidth σ. The solid lines are best fits using (27) in (*b*) and to a constant dependence on δ/σ in (*c*). Image from [59].

9. Conclusions

We reviewed above optical methods for controlling quantum dot (QD) spins in general and exciton spins in particular.

We first briefly discussed the growth process for self-assembled semiconductor QDs. We then outlined the experimental techniques used to characterize single self-assembled QDs and to probe the dynamics of confined carriers in them. Characteristic optical studies were then compared with a detailed many carrier model used to comprehensively understand the rich one- and two-pulse photoluminescence and photoluminescence excitation spectra of single QDs. We then demonstrated how the polarization of a short laser pulse is translated with high fidelity into a coherent state of the exciton spin. We concluded by reviewing an all-optical method which enables full coherent control over the exciton spin using a single, picosecond long resonant optical pulse. We showed that this coherent control can be conveniently described geometrically as a rotation of the exciton spin state vector around the direction of the optical pulse polarization, while the angle of rotation is fully defined by the amount by which the pulse is detuned from resonance. The method presented above should be applicable to other qubit systems as well, including but not limited to nitrogen-vacancy centres in diamonds [124]. The only requirement is an optical transition to a non-degenerate auxiliary level or a truly Λ system.

Acknowledgments

The support of the US-Israel Binational Science Foundation (BSF), the Israeli Science Foundation (ISF), the Israeli Nanotechnology Focal Technology Area and that of the Technions RBNI are gratefully acknowledged.

References

[1] Shor P W 1994 Algorithms for quantum computation: discrete logarithms and factoring *SFCS'94: Proc. of the 35th Annual Symp. on Foundations of Computer Science* (Washington, DC: IEEE Computer Society Press) p 124

[2] Grover L K 1996 A fast quantum mechanical algorithm for database search *STOC'96: Proc. of the 28th Annu. ACM Symp. on Theory of Computing* (New York, NY: ACM) p 212

[3] Bennett C H and Brassard G 1984 Quantum cryptography: public key distribution and coin tossing *Proc. of IEEE Int. Conf. on Computers Systems and Signal Processing* p 175

[4] Ekert A K 1991 Quantum cryptography based on Bell's theorem *Phys. Rev. Lett.* **67** 661

[5] Peev M *et al* 2009 The SECOQC quantum key distribution network in Vienna *New J. Phys.* **11** 075001

[6] Nielsen M A and Chuang I L 2004 *Quantum Computation and Quantum Information (Cambridge Series on Information and the Natural Sciences)* 1st edn (Cambridge: Cambridge University Press)

[7] DiVincenzo D P 2000 *Fortschr. Phys.* **48** 771–83

[8] Barenco A, Bennett C H, Cleve R, DiVincenzo D P, Margolus N, Shor P, Sleator T, Smolin J A and Weinfurter H 1995 *Phys. Rev.* A **52** 3457

[9] Lloyd S 1995 *Phys. Rev. Lett.* **75** 346–9

[10] Barenco A and Dupertuis M A 1995 *Phys. Rev.* B **52** 2766

[11] Monz T, Kim K, Hansel W, Riebe M, Villar A S, Schindler P, Chwalla M, Hennrich M and Blatt R 2009 *Phys. Rev. Lett.* **102** 040501

[12] Cory D G, Price M D, Maas W, Knill E, Laflamme R, Zurek W H, Havel T F and Somaroo S S 1998 *Phys. Rev. Lett.* **81** 2152–5

[13] Fedorov A, Seffen L, Baur M, da Silva M P and Wallraff A 2012 *Nature* **481** 170–2

[14] Lanyon B P, Barbieri M, Almeida M P, Jennewein T, Ralph T C, Resch K J, Pryde G J, O'Brien J L, Gilchrist A and White A G 2009 *Nature Phys.* **5** 134–40

[15] Ladd T D, Jelezko F, Laflamme R, Nakamura Y, Monroe C and O'Brien J L 2010 *Nature* **464** 45

[16] Monz T, Schindler P, Barreiro J T, Chwalla M, Nigg D, Coish W A, Harlander M, Hänsel W, Hennrich M and Blatt R 2011 *Phys. Rev. Lett.* **106** 130506

[17] Anderlini M, Lee P J, Brown B L, Sebby-Strabley J, Phillips W D and Porto J V 2007 *Nature* **448** 452

[18] Vandersypen L M K, Steffen M, Breyta G, Yannoni C S, Sherwood M H and Chuang I L 2001 *Nature* **414** 883–7

[19] Negrevergne C, Mahesh T S, Ryan C A, Ditty M, Cyr-Racine F, Power W, Boulant N, Havel T, Cory D G and Laflamme R 2006 *Phys. Rev. Lett.* **96** 170501

[20] DiCarlo L *et al* 2009 *Nature* **460** 240–4

[21] Dutt M V G, Childress L, Jiang L, Togan E, Maze J, Jelezko F, Zibrov A S, Hemmer P R and Lukin M D 2007 *Science* **316** 1312

[22] Loss D and DiVincenzo D P 1998 *Phys. Rev.* A **57** 120–6

[23] Kastner M A 1993 *Phys. Today* **46** 24

[24] Gammon D 2000 *Nature* **405** 899–900

[25] Crowley M T, Naderi N A, Su H, Grillot F and Lester L F 2012 Gaas-based quantum dot lasers *Advances in Semiconductor Lasers (Semiconductors and Semimetals* vol 86*)* ed J J Coleman and A C Bryce (San Diego, CA: Academic) pp 371–417

[26] Bimberg D, Grundmann M and Ledentsov N N 1999 *Quantum Dot Heterostructures* (New York: Wiley)

[27] Petta J R, Johnson A C, Taylor J M, Laird E A, Yacoby A, Lukin M D, Marcus C M, Hanson M P and Gossard A C 2005 *Science* **309** 2180–4

[28] Koppens F H L, Buizert C, Tielrooij K J, Vink I T, Nowack K C, Meunier T, Kouwenhoven L P and Vandersypen L M K 2006 *Nature* **442** 766–71

[29] Schinner G J, Repp J, Schubert E, Rai A K, Reuter D, Weick A D, Govorov A O, Holleitner A W and Kotthaus J P 2013 *Phys. Rev. Lett.* **110** 127403

[30] Dekel E, Gershoni D, Ehrenfreund E, Garcia J M and Petroff P M 2000 *Phys. Rev.* B **61** 11009

[31] Dekel E, Regelman D V, Gershoni D, Ehrenfreund E, Schoenfeld W V and Petroff P M 2000 *Phys. Rev.* B **62** 11038

[32] Michler P, Kiraz A, Becher C, Schoenfeld W V, Petroff P M, Zhang L, Hu E and Imamoglu A 2000 *Science* **290** 2282

[33] Santori C, Pelton M, Solomon G, Dale Y and Yamamoto Y 2001 *Phys. Rev. Lett.* **86** 1502

[34] Dekel E, Regelman D V, Gershoni D, Ehrenfreund E, Schoenfeld W V and Petroff P M 2001 *Solid State Commun.* **117** 395

[35] Regelman D V, Mizrahi U, Gershoni D, Ehrenfreund E, Schoenfeld W V and Petroff P M 2001 *Phys. Rev. Lett.* **87** 257401

[36] Akopian N, Lindner N H, Poem E, Berlatzky Y, Avron J, Gershoni D, Gerardot B D and Petroff P M 2006 *Phys. Rev. Lett.* **96** 130501

[37] Hafenbrak R, Ulrich S M, Michler P, Wang L, Rastelli A and Schmidt O G 2007 *New J. Phys.* **9** 315

[38] Young R J, Stevenson R M, Atkinson P, Cooper K, Ritchie D A and Shields A J 2006 *New J. Phys.* **8** 29

[39] De Greve K *et al* 2012 *Nature* **491** 421–6

[40] Gao W B, Hallahi P, Togan E, Miguel-Sanchez J and Imamoglu A 2012 *Nature* **491** 426–30

[41] Schaibley J R, Burgers A P, McCracken G A, Duan L-M, Berman P R, Steel D G, Bracker A S, Gammon D and Sham L J 2013 *Phys. Rev. Lett.* **110** 167401

[42] Kim D, Bracker A S, Carter S G, Greilich A and Gammon D 2011 *Nature Phys.* **7** 223–9

[43] Gao W B, Fallahi P, Togan E, Delteil A, Chin Y S, Miguel-Sanchez J and Imamoglu A 2013 *Nature Commun.* **4** 2744

[44] Strauf S, Stoltz N G, Rakher M T, Coldren L A, Petroff P M and Bouwmeester D 2007 *Nature Photon.* **1** 704

[45] Dousse A, Suffczynski J, Beveratos A, Krebs O, Lemaitre A, Sagnes I, Bloch J, Voisin P and Senellart P 2010 *Nature* **466** 217

[46] Berezovsky J, Mikkelsen M H, Stoltz N G, Coldren L A and Awschalom D D 2008 *Science* **320** 349

[47] Press D, Ladd T D, Zhang B and Yamamoto Y 2008 *Nature* **456** 218

[48] Economou S E, Sham L J, Wu Y and Steel D G 2006 *Phys. Rev.* B **74** 205415

[49] Economou S E and Reinecke T L 2007 *Phys. Rev. Lett.* **99** 217401

[50] Greilich A, Economou S E, Spatzek S, Yakovlev D R, Reuter D, Wieck A D, Reinecke T L and Bayer M 2009 *Nature Phys.* **5** 262

[51] Kim E D, Truex K, Xu X, Sun B, Steel D G, Bracker A S, Gammon D and Sham L J 2010 *Phys. Rev. Lett.* **104** 167401

[52] Kim D, Carter S G, Greilich A, Bracker A S and Gammon D 2011 *Nature Phys.* **7** 223

[53] Godden T M, Quilter J H, Ramsay A J, Wu Y, Brereton P, Boyle S J, Luxmoore I J, Puebla-Nunez J, Fox A M and Skolnick M S 2012 *Phys. Rev. Lett.* **108** 017402

[54] De Greve K *et al* 2011 *Nature Phys.* **7** 872–8

[55] Bracker A S *et al* 2005 *Phys. Rev. Lett.* **94** 047402

[56] Fras F, Eble B, Desfonds P, Bernardot F, Testelin C, Chamarro M, Miard A and Lemaitre A 2011 *Phys. Rev.* B **84** 125431

[57] Benny Y, Khatsevich S, Kodriano Y, Poem E, Presman R, Galushko D, Petroff P M and Gershoni D 2011 *Phys. Rev. Lett.* **106** 040504

[58] Poem E, Kenneth O, Kodriano Y, Benny Y, Khatsevich S, Avron J E and Gershoni D 2011 *Phys. Rev. Lett.* **107** 087401

[59] Kodriano Y, Schwartz I, Poem E, Benny Y, Presman R, Truong T A, Petroff P M and Gershoni D 2012 *Phys. Rev.* B **85** 241304

[60] Poem E, Shemesh J, Marderfeld I, Galushko D, Akopian N, Gershoni D, Gerardot B D, Badolato A and Petroff P M 2007 *Phys. Rev.* B **76** 235304

[61] Benny Y, Kodriano Y, Poem E, Gershoni D, Truong T A and Petroff P M 2012 *Phys. Rev.* B **86** 085306

[62] Snyder C W, Orr B G, Kessler D and Sander L M 1991 *Phys. Rev. Lett.* **66** 3032

[63] Saito H, Nishi K and Sugou S 1999 *App. Phys. Lett.* **74** 1224–6

[64] Venables J A 2000 *Introduction to Surface and Thin Film Processes* (Cambridge: Cambridge University Press)

[65] Markov I V 1995 *Crystal Growth for Beginners: Fundamentals of Nucleation, Crystal Growth, and Epitaxy* (Singapore: World Scientific)

[66] Venables J A, Spiller G D T and Hanbucken M 1984 *Rep. Prog. Phys.* **47** 399–459

[67] Warburton R J 2002 *Contemp. Phys.* **43** 351

[68] Leonard D, Pond K and Petroff P M 1994 *Phys. Rev.* B **50** 11687

[69] Zolotaryov A, Schramm A, Heyn C and Hansen W 2007 *Appl. Phys. Lett.* **91** 083107

[70] Joyce P B, Krzyzewski T J, Bell G R and Jones T S 2000 *Phys. Rev.* B **62** 10551

[71] Malik S, Roberts C, Murray R and Pate M 1997 *Appl. Phys. Lett.* **14** 1987

[72] Le Ru E C, Fack J and Murray R 2003 *Phys. Rev.* B **67** 245318

[73] Garcia J M, Mankad T, Holtz P O, Wellman P J and Petroff P M 1998 *Appl. Phys. Lett.* **72** 3172

[74] Garcia J M, Medeiros-Ribeiro G, Schmidt K, Ngo T, Feng J L, Lorke A, Kotthaus J and Petroff P M 1997 *Appl. Phys. Lett.* **71** 2014

[75] Ramon G, Mizrahi U, Akopian N, Braitbart S, Gershoni D, Reinecke T L, Gerardot B D and Petroff P M 2006 *Phys. Rev.* B **73** 205330
[76] Benny Y, Kodriano Y, Poem E, Khatsevitch S, Gershoni D and Petroff P M 2011 *Phys. Rev.* B **84** 075473
[77] Poem E and Gershoni D 2011 Radiative cascades in semiconductor quantum dots *Handbook of Luminescent Semiconductor Materials* ed L Bergman and J L McHale (Boca Raton, FL: CRC Press) pp 321–64
[78] Moreau E, Robert I, Manin L, Thierry-Mieg V, Gérard J M and Abram I 2001 Quantum cascade of photons in semiconductor quantum dots *Phys. Rev. Lett.* **87** 183601
[79] Poem E, Kodriano Y, Tradonsky C, Gerardot B D, Petroff P M and Gershoni D 2010 *Phys. Rev.* B **81** 085306
[80] Kodriano Y, Poem E, Lindner N H, Tradonsky C, Gerardot B D, Petroff P M, Avron J E and Gershoni D 2010 *Phys. Rev.* B **82** 155329
[81] Michler P, Imamoglu A, Mason M D, Carson P J, Strouse G F and Buratto S K 2000 *Nature* **406** 968–70
[82] Zwiller V, Blom H, Jonsson P, Panev N, Jeppesen S, Tsegaye T, Goobar E, Pistol M-E, Samuelson L and Bjork G 2001 *Appl. Phys. Lett.* **78** 2476–8
[83] Yuan Z, Kardynal B, Stevenson R M, Shields A J, Lobo C J, Cooper K, Beattie N S, Ritchie D A and Pepper M 2002 *Science* **295** 102–50
[84] Baier M H, Malko A, Pelucchi E, Oberli D Y and Kapon E 2006 *Phys. Rev.* B **73** 205321
[85] Poem E, Kodriano Y, Tradonsky C, Lindner N H, Gerardot B D, Petroff P M and Gershoni D 2010 *Nature Phys.* **6** 993
[86] Brown R H and Twiss R Q 1956 *Nature* **178** 1046
[87] Gershoni D, Henry C H and Baraff G A 1993 *IEEE J. Quantum Electron.* **29** 2433–50
[88] Pryor C 1998 *Phys. Rev.* B **57** 7190–5
[89] Bester G, Selvakumar N and Zunger A 2003 *Phys. Rev.* B **67** 161306
[90] Warburton R J, Miller B T, Dürr C S, Bödefeld C, Karrai K, Kotthaus J P, Medeiros-Ribeiro G, Petroff P M and Huant S 1998 *Phys. Rev.* B **58** 16221
[91] Jensen F 2007 *Introduction to Computational Chemistry* (New York: Wiley)
[92] Ivchenko E L and Pikus G 1997 *Superlattices and Other Heterostructures: Symmetry and Optical Phenomena (Springer Series in Solid-State Sciences)* 2nd edn (Berlin: Springer)
[93] Bayer M *et al* 2002 *Phys. Rev.* B **65** 195315
[94] Takagahara T 2000 *Phys. Rev.* B **62** 16840
[95] Alon-Braitbart S *et al* 2006 *Proc. of the 12th Int. Conf. on Modulated Semiconductor Structures; Physica* E **32** 127–30
[96] Gammon D, Snow E S, Shanabrook B V, Katzer D S and Park D 1996 *Phys. Rev. Lett.* **76** 3005
[97] Bastard G 1991 *Wave Mechanics Applied to Semiconductor Heterostructures* 1st edn (New York: Wiley-Interscience)
[98] Miller R C, Gossard A C, Sanders G D, Chang Y-C and Schulman J N 1985 *Phys. Rev.* B **32** 8452
[99] Warming T, Siebert E, Schliwa A, Stock E, Zimmermann R and Bimberg D 2009 *Phys. Rev.* B **79** 125316
[100] Siebert E, Warming T, Schliwa A, Stock E, Winkelnkemper M, Rodt S and Bimberg D 2009 *Phys. Rev.* B **79** 205321
[101] Ediger M, Bester G, Badolato A, Petroff P M, Karrai K, Zunger A and Warburton R J 2007 *Nature Phys.* **3** 774
[102] Maialle M Z and Degani M H 2007 *Phys. Rev.* B **76** 115302
[103] Kavokin K V 2003 *Phys. Status Solidi* a **195** 592
[104] Akimov I A, Kavokin K V, Hundt A and Henneberger F 2005 *Phys. Rev.* B **71** 075326
[105] Hameau S, Guldner Y, Verzelen O, Ferreira R, Bastard G, Zeman J, Lemaître A and Gérard J M 1999 *Phys. Rev. Lett.* **83** 4152
[106] Sarkar D, van der Meulen H P, Calleja J M, Becker J M, Haug R J and Pierz K 2005 *Phys. Rev.* B **71** 081302
[107] Sarkar D, van der Meulen H P, Calleja J M, Meyer J M, Haug R J and Pierz K 2008 *Appl. Phys. Lett.* **92** 181909
[108] Lemaître A, Ashmore A D, Finley J J, Mowbray D J, Skolnick M S, Hopkinson M and Krauss T F 2001 *Phys. Rev.* B **63** 161309
[109] Findeis F, Zrenner A, Böhm G and Abstreiter G 2000 Phonon-assisted biexciton generation in a single quantum dot *Phys. Rev.* B **61** R10579
[110] Claudon J, Bleuse J, Malik N S, bazin M, Jaffrennou P, Gregersen N, Sauvan C, Lalanne P and Gerard J M 2010 *Nature Photon.* **4** 174–7
[111] Zrenner A, Beham E, Stufler S, Findeis F, Bichler M and Abstreiter G 2002 *Nature* **418** 612–4
[112] Muller K, Kaldewey T, Ripszam R, Wildmann J S, Bechtold A, Bichler M, Koblmuller g, Abstreiter G and Finley J J 2013 *Sci. Rep.* **3** 1906
[113] Finley J J, Ashmore A D, Lemaître A, Mowbray D J, Skolnick M S, Itskevich I E, Maksym P A, Hopkinson M and Krauss T F 2001 *Phys. Rev.* B **63** 073307
[114] Wu Y, Kim E D, Xu X, Cheng J, Steel D G, Bracker A S, Gammon D, Economou S E and Sham L J 2007 *Phys. Rev. Lett.* **99** 097402
[115] Bonadeo N H, Erland J, Gammon D, Park D, Katzer D S and Steel D G 1998 *Science* **282** 1473
[116] Flissikowski T, Hundt A, Lowisch M, Rabe M and Henneberger F 2001 *Phys. Rev. Lett.* **86** 3172
[117] Boyle S J, Ramsay A J, Bello F, Liu H Y, Hopkinson M, Fox A M and Skolnick M S 2008 *Phys. Rev.* B **78** 075301
[118] Rosen N and Zener C 1932 *Phys. Rev.* **40** 502
[119] Takagahara T 2010 *J. Opt. Soc. Am. B* **27** A46
[120] Ramsay A J, Boyle S J, Kolodka R S, Oliveira J B B, Skiba-Szymanska J, Liu H Y, Hopkinson M, Fox A M and Skolnick M S 2008 *Phys. Rev. Lett.* **100** 197401
[121] de la Giroday A B, Bennett A J, Pooley M A, Stevenson R M, Sköld N, Patel R B, Farrer I, Ritchie D A and Shields A J 2010 *Phys. Rev.* B **82** 241301
[122] de Vasconcellos S M, Gordon S, Bichler M, Meier T and Zrenner A 2010 *Nature Photon.* **4** 545–8
[123] Imamoğlu A, Awschalom D D, Burkard G, DiVincenzo D P, Loss D, Sherwin M and Small A 1999 *Phys. Rev. Lett.* **83** 4204–7
[124] Buckley B B, Fuchs G D, Bassett L C and Awschalom D D 2010 *Science* **330** 1212–5